

# PROPAGATING STAR FORMATION IN THE COLLISIONAL RING GALAXY ARP 10

BIZYAEV D.V.<sup>1,2</sup>, MOISEEV A.V.<sup>3</sup>, AND VOROBYOV E.I.<sup>4,5</sup>

*Draft version October 5, 2018*

## ABSTRACT

Propagating star formation in a collisional ring galaxy Arp 10 is investigated by a complex approach, which includes the broad- and narrow-band photometry, long-slit spectroscopy, and scanning Fabry-Perot spectroscopy. The ionized gas velocity field obtained with best spatial resolution to date indicates a non-isotropic expansion of the outer ring with a maximum velocity  $110 \text{ km s}^{-1}$ . Strong vertical and non-circular motions are also seen in the vicinity of the inner ring. Our kinematic data suggest that Arp 10 has a small inclination  $i = 22^\circ$  and high total (luminous plus dark matter) mass of about  $10^{12} M_\odot$  within a 50 kpc radius. The internal extinction in HII regions and extinction-corrected H $\alpha$  fluxes are estimated from the emission lines. The abundance of oxygen  $12 + \log(\text{O}/\text{H})$  in both star-forming rings is about 8.6. The analysis of spectral indices provides an estimate on the propagation velocities of both rings and metallicity of the pre-collision stellar population. A small "knot" near the nucleus of Arp 10, which was previously suspected as a possible candidate for collision, is now unambiguously identified as the "intruder". The intruder spectrum suggests that it was a spiral galaxy before the collision and its present mass amounts to at least one-fourth of the total mass of Arp 10. A high value of the intruder velocity relative to Arp 10 ( $\approx 480 \text{ km s}^{-1}$ ) suggests that the intruder is either gravitationally unbound or marginally bound to the main galaxy. We use a simplified two-dimensional hydrodynamic modeling of galaxy collisions to test a collisional origin of Arp 10. We confirm that the sizes of the inner and outer rings, maximum expansion velocity of the outer ring, and radial profile of the gas circular velocity can be reproduced by a near-central collision with the intruder galaxy, which occurred approximately 85 Myr ago. We acknowledge that an apparent crescent-shaped distribution of H $\alpha$  emission in the outer ring is caused by a star formation threshold in the gas disk of Arp 10.

*Subject headings:* galaxies: general — abundances, galaxies: individual(Arp 10)

## 1. INTRODUCTION

Collisional ring galaxies (Vorontsov-Veliaminov 1976) give us a bright example of star formation induced by radially expanding density waves, which are triggered by a near-axial passage of a companion galaxy through the disk of a target galaxy (Lynds & Toomre 1976; Higdon 1995; Charmandaris & Appleton 1996). The expanding density waves in the gas disk of a target galaxy leave behind stellar populations of progressively older age. This allows us to study the sequence of large-scale star formation events by considering adjacent locations along the galactic radius. A sequential triggering of star formation by expanding density waves makes collisional ring galaxies a unique laboratory for studying young stellar populations.

The best studied collisional ring galaxy to date is the Cartwheel. Star formation in the Cartwheel is concentrated in the two rings, which reveal the presence of expanding density waves (Higdon 1995, 1996; Appleton & Struck-Marcell 1996). The non-stationary and propagating nature of star formation is manifested by the current radial expansion of the rings (Higdon 1996; Amram et al. 1998; Vorobyov & Bizyaev 2003), radial

color gradients (Markum et al 1992; Borne et al. 1997; Korchagin et al. 2001; Vorobyov & Bizyaev 2001), and radial age distribution of young stellar clusters (Appleton 1999). However, the nature of the pre-collision Cartwheel is still controversial: it might have been either a gas-rich low surface brightness galaxy (Korchagin et al. 2001) or a regular large galaxy (Vorobyov & Bizyaev 2003). To identify the types of disk galaxies that can serve progenitors to the collisional ring galaxies, we should extend the observational and theoretical studies beyond the Cartwheel.

The available sample of collisional ring galaxies, i.e. galaxies with an apparent ring morphology and nearby companions, is relatively small. However, traces of expanding rings and associated star formation can be found in otherwise regular galaxies. These features include a shift between the peaks of radial distributions of OB-associations and HII regions in M 51, M 101, and some other nearby galaxies (Smirnov & Komberg 1976), recently discovered ring in NGC 922 (Wong et al. 2006), and ring-like structure in the inner region of M 31 (Block et al. 2006). This evidence suggests that head-on collisions with satellites are likely to be a more frequent phenomenon in the local universe than they were previously thought.

This paper is motivated by the fact that propagating waves of star formation are expected to leave behind stellar populations, the ages of which should be characterized by a radial gradient. This gradient should be imprinted in the absorption spectra measured at different radial distances from the center of a collisional ring

Electronic address: dmbiz@noao.edu, moisav@sao.ru, vorobyov@astro.uva.nl

<sup>1</sup> National Optical Astronomy Observatory, Tucson, AZ, 85719

<sup>2</sup> Sternberg Astronomical Institute, Moscow, 119899, Russia

<sup>3</sup> Special Astrophysical Observatory, Nizhniy Arkhyz, Karachaevo-Cherkessiya, Russia

<sup>4</sup> CITA National Fellow, The University of Western Ontario, London, Canada

<sup>5</sup> Institute of Physics, Stachki 194, Rostov-on-Don, Russia

galaxy. We have chosen Arp 10, a galaxy with an apparent ring morphology, because of its large size and convenient location for our observations (in the Northern Hemisphere). Unlike the Cartwheel, Arp 10 shows clear signs of the old stellar population in the form of elements of spiral arms and prominent bulge. This gives us an opportunity to study the development of ring structures in regular spiral galaxies. In contrast to previous works (Charmandaris et al. 1993; Marston & Appleton 1995; Charmandaris & Appleton 1996; Bransford et al. 1998), we considerably improved the spatial resolution of kinematical studies of Arp 10. We also search for the companion that is presumably responsible for the Arp 10 peculiar ring structure. The new set of observational data allows us to create a self-consistent picture of collision and subsequent star formation in Arp 10.

## 2. OBSERVATIONS

Observations of Arp 10 were conducted with the 6-meter telescope at the Special Astrophysical Observatory (Russian Academy of Sciences) and multi-mode focal reducer SCORPIO (see Afanasiev & Moiseev 2005, for details). The SCORPIO allows us to carry out the broad- and narrow-band photometry, long-slit spectroscopy, and scanning Fabry-Perot spectroscopy. The detector is a  $2048 \times 2048$  pixels CCD EEV42-20.

### 2.1. Photometry

The  $H\alpha$  and Johnson-Cousins B- and R-images were taken on September 21/22, 2003. The pixel size was 0.36 arcsec (with binning  $2 \times 2$ ). We obtained several dithered images in each broadband filter, with a total integration time 600 and 70 sec in the B and R-bands, respectively. The mean seeing was 1.6 arcsec. The images were corrected for bias and flat field, cosmic ray hits, and sky background. A saturated nucleus in the B- and R-bands was corrected using short exposures. The B-band image is shown in Figure 1.

To obtain the  $H\alpha$  image corrected for the continuum, we used the  $15 \text{ \AA}$  filter centered at  $6720 \text{ \AA}$  for the emission line and  $15 \text{ \AA}$  filter centered at  $6765 \text{ \AA}$  for the continuum. The images in these filters were integrated for 1200 and 600 sec for the  $H\alpha$  and continuum, respectively. The  $H\alpha$  image of Arp 10 corrected for the continuum and superimposed onto the B-band image is shown in Figure 2.

### 2.2. Long-slit spectroscopy

We obtained three long-slit spectra of Arp 10 using a 1.0 arcsec wide slit. The spectra are taken along three cuts, which pass through the center of the galaxy and are shown in Figure 2. The summary of spectral observations including the supplementary information about the spectral range and resolution, corresponding integration times, and position angles of the cuts are given in Table 1. The first spectral cut coincides with the major axis of the outer ring in Arp 10. The second cut is drawn at the position angle  $118^\circ$  and covers a larger spectral range with a lower spectral resolution. The third cut passes through a small "knot" (presumable satellite-intruder) at 5 arcsec from the center of the galaxy. The spectra were reduced by the standard procedure (bias subtraction, flat fielding, night sky subtraction, and wavelength calibration), and then flux-calibrated with the help of standard

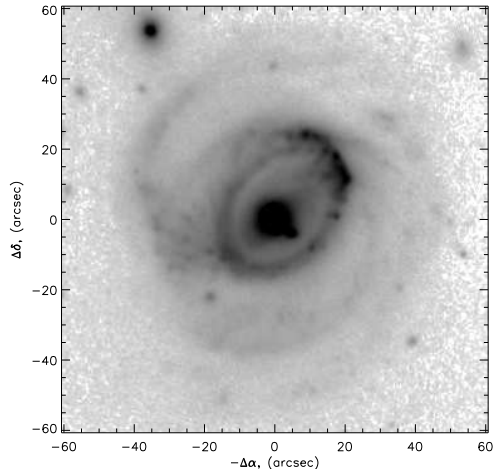


FIG. 1.— B-band image of Arp 10.

TABLE 1  
SUMMARY OF SCORPIO LONG-SLIT OBSERVATIONS

#	Date	Sp. Range Å	Sp. Resol. Å	Exp. time sec	P.A.
1	Sep. 21/22, 2003	4150-5890	5	6000	$138^\circ$
2	Nov. 02/03 2003	3700-7400	8	4800	$118^\circ$
3	Aug. 16/17, 2004	4040-5600	5	2700	$50^\circ$

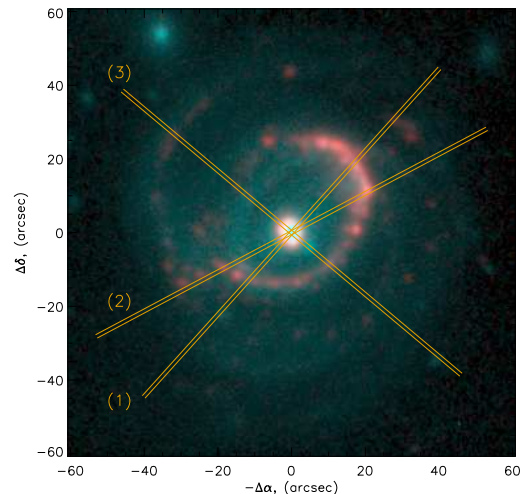


FIG. 2.—  $H\alpha$  image of Arp 10 (red) superimposed on the B-image (blue). Positions of the long-slit cuts are shown by solid lines. The cuts are labelled according to the text.

stars BD+75 325 and BD+25 4655. The dispersion of the spectra along the cuts is  $0.71 \text{ arcsec pix}^{-1}$ . The seeing was 1.4-1.6 arcsec during the observations. The one-dimensional spectra of regions within the outer ring, inner ring, and center of Arp 10 are shown in Figure 3.

### 2.3. Fabry-Perot Spectroscopy

The  $H\alpha$  velocity field of Arp 10 was obtained via 7320 seconds of integration with the SCORPIO in the

scanning Fabry-Perot Interferometer (FPI) mode with 32 spectral channels. Each channel corresponds to  $40 \text{ km s}^{-1}$ . The formal accuracy of our radial velocity measurements obtained from the  $H\alpha$  line fitting by a Gaussian is  $10 \text{ km s}^{-1}$ . The typical procedure of reduction of the FPI frames is described in detail by Moiseev (2002). The spatial sampling of  $0.71 \text{ arcsec pix}^{-1}$  and velocity resolution of  $125 \text{ km s}^{-1}$  are achieved in our frames. The data were smoothed to the spatial resolution corresponding to a seeing  $2.9 \text{ arcsec}$ .

### 3. STRUCTURE OF ARP 10 FROM THE B AND $H\alpha$ PHOTOMETRY.

The broad-band images of Arp 10 indicate the presence of an exponential disk and prominent bulge. We fit the R-band image with a model exponential disk and bulge (see for details Smirnova et al. 2006) and obtain the following parameters: the exponential disk scale length is  $11.4 \text{ arcsec}$  and exponential bulge scale length is  $2.8 \text{ arcsec}$ . These scales correspond to  $7.18 \text{ kpc}$  and  $1.77 \text{ kpc}$ , respectively, for the adopted distance of  $130 \text{ Mpc}$  ( $H_0 = 70 \text{ km s}^{-1} \text{ Mpc}^{-1}$ ). One arcsec corresponds to  $0.63 \text{ kpc}$  and the ratio of the bulge-to-disk luminosities is  $0.4$ .

The  $H\alpha$  emission of Arp 10 comes mostly from two star forming rings, which are clearly seen in Figure 2. However, the  $H\alpha$  structure is more complicated than is expected from a simplified picture, in which a star formation wave propagates from the center toward the periphery. The outer ring is rather asymmetric, with the  $H\alpha$  emission coming mostly from its North-Western part (top-right in Figure 2). At the same time, the inner ring has a concentric shape. A long arc of star-forming regions that traces an outer spiral arm joins the outer ring in its South-Eastern part (bottom-left in Figure 2). A similar but a fainter arc is seen on the opposite side of Arp 10.

The structure of the outer disk is best seen in the B-band image (Figure 1). Outside the outer ring, at least three spiral arms can be identified, two of them are revealed in the  $H\alpha$  image. The diameter of the outer  $H\alpha$  ring ( $28 \text{ kpc}$ ) is twice smaller than  $D_{25} = 57 \text{ kpc}$  (according to de Vaucouleurs et al. 1991). This is in agreement with recent multi-band photometry of 15 northern ring galaxies by Romano et al. (2007), who have found that stellar disks extend outside  $H\alpha$  emitting rings in all galaxies of their sample. Figure 1 suggests that the pre-collision Arp 10 might have possessed a complicated structure typical for spiral galaxies.

### 4. KINEMATICS OF ARP 10

In this section we derive the kinematics of Arp 10 using the long-slit and FPI spectroscopy. Figure 4 shows the  $H\alpha$ , [OIII], and stellar line-of-sight velocities for our long-slit data (top panel) taken along the first cut. The velocities in Figure 4 are not corrected for inclination. It can be noticed that at some radii stars rotate faster than the ionized gas, which indicates a presence of essential non-circular motions in the galaxy. The bottom panel in Figure 4 demonstrates the stellar velocity dispersion distribution, which is typical for very large spiral galaxies with high amplitudes of rotation curves (van der Kruit & Freeman 1986; Bottenga 1993).

The two-dimensional  $H\alpha$  velocity field of Arp 10 was analyzed by a tilted-ring technique in the same manner as

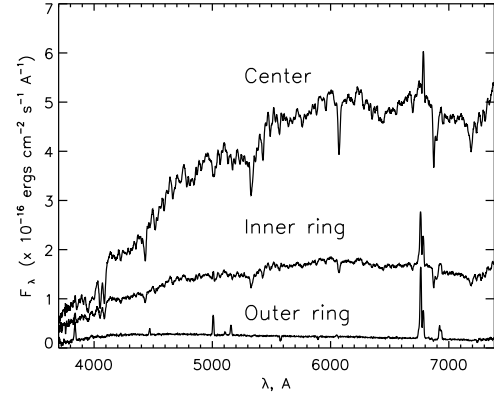


FIG. 3.— One-dimensional spectra of regions within the outer ring, inner ring, and center of Arp 10 from our long-slit spectroscopy (cut 2).

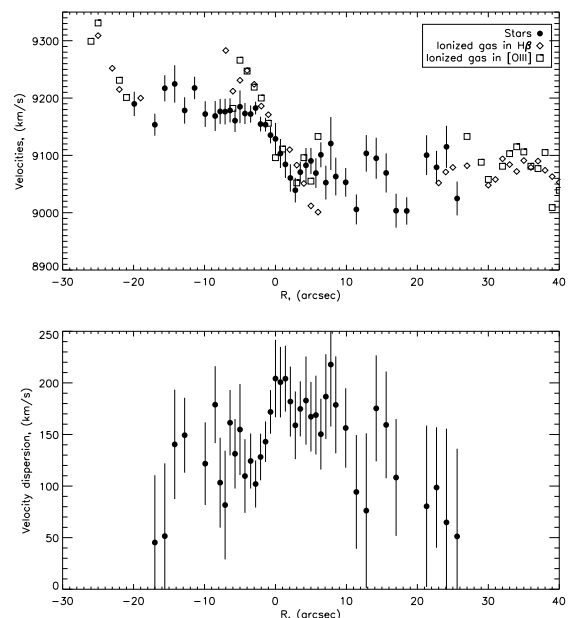


FIG. 4.— Line-of-sight velocities (*top panel*) of Arp 10 obtained with the long-slit spectroscopy. The ionized gas velocities are shown by diamonds ( $H\beta$ ) and squares ([OIII]). Stellar velocities are designated by filled circles. Radial distribution of the stellar velocity dispersion is shown in the *bottom panel*.

described by Smirnova et al. (2006). A similar technique was applied to the Cartwheel galaxy by (Amram et al. 1998) and to Arp 10 by Charmandaris & Appleton (1996). In contrast to our analysis, Charmandaris & Appleton used low-resolution HI data.

To analyze the velocity field of Arp 10 shown in Figure 5, we assume that the line-of-sight velocity of the ionized gas  $V_{obs}$  is a combination of the following four components: a systematic velocity  $V_{sys}$ , azimuthal velocity in the plane of the disk  $V_\phi$ , radial expansion velocity in the plane of the disk  $V_r$ , and vertical velocity  $V_z$ :

$$V_{obs} = V_{sys} + V_\phi \cos \phi \sin i + V_r \sin \phi \sin i + V_z \cos i. \quad (1)$$

Here  $i$  designates the inclination of the galactic plane and  $\phi$  denotes the azimuthal angle, which is measured counterclockwise from the major axis. The position angle of an arbitrary point in the disk p.a. is connected with

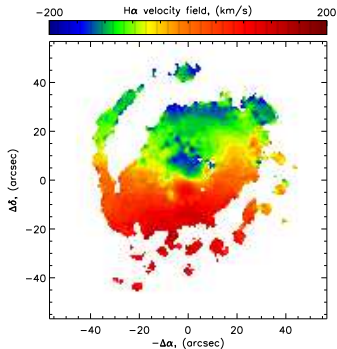


FIG. 5.— Two-dimensional velocity field in Arp 10 obtained with the scanning FPI analysis.

angle  $\phi$  as  $\tan(\text{p.a.} - \text{P.A.}) = \tan(\phi) \cos(i)$ , where P.A. is position angle of the major axis (line-of-nodes). We split the galactic disk of Arp 10 into 48 tilted circular annuli. In the case of a purely circular motion (P.A.=const,  $i$ =const,  $V_r = 0$ , and  $V_z = 0$ ), the best fit position angle of the major axis and inclination are  $172 \pm 2^\circ$  and  $22 \pm 4^\circ$ . We obtained these values by masking the inner and outer rings.

The mean rotation curve of Arp 10 is derived from our two-dimensional  $H\alpha$  velocity field and is shown by the points in the upper panel of Figure 6. Next, we use an assumption of quasi-circular motions and calculate P.A. independently in each elliptical annulus. The points in the middle panel of Figure 6 show P.A. at different distances from the center of Arp 10. The points in the bottom panel represent a sum of the systematic and vertical components of the line-of-sight velocity. We note that the rotation curve continues to rise slowly even at large radii (50 arcsec, or 32 kpc). The dashed lines in all three panels of Figure 6 show the values that are used to construct the model velocity field using equation (1). This field is presented in the top panel of Figure 7. The model velocity field was subtracted from the observed velocity field to obtain the residual velocity field, which is shown in the bottom panel of Figure 7.

The kinematic data suggest that the best-fit inclination is  $22^\circ$  rather than the photometric inclination  $49^\circ$  used by Charmandaris & Appleton (1996). Taking into consideration the asymmetric shape of the outer ring in Arp 10, this large difference in the values of inclination is not surprising. Reshetnikov (1999) noticed that Arp 10 would not fit into a general Tully-Fisher relation, if an inclination of  $i = 49^\circ$  is adopted. A lower value of inclination  $i = 22^\circ$  that provides better agreement with the Tully-Fisher diagram suggests a total mass of Arp 10 to be  $7 \times 10^{11} M_\odot$  within a radius of 30 kpc. The value of the kinematic position angle of the major axis  $172^\circ$  is in poor agreement with the value  $125^\circ$  derived from the photometric data (Paturel et al. 2003). Assuming that the outer spirals in Figure 1 are trailing, we conclude that the galaxy rotates counterclockwise and its Eastern part (the left half in Figure 2 and Figure 5) is closest to us.

The residual velocity field of Figure 7 and radial variations of P.A. and  $V_z \cos i$  in Figure 6 indicate the presence of two main features.

1) Velocities in the inner ring suggest significant verti-

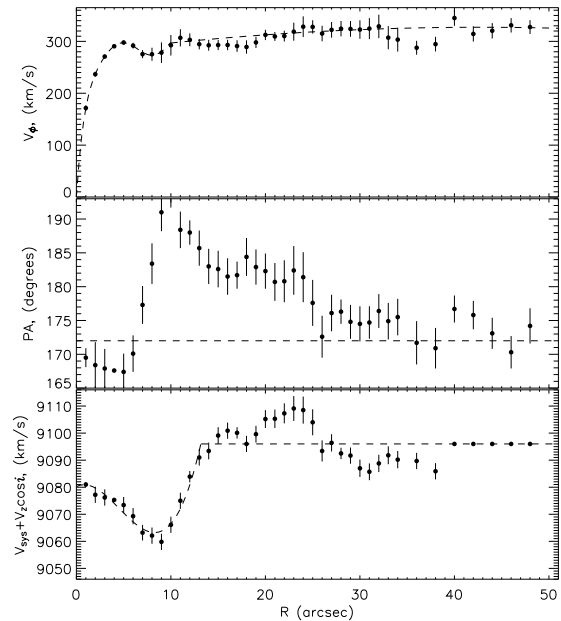


FIG. 6.— Tilted-rings analysis of the velocity field in Arp 10. *Top panel*: Rotation curve with error bars (circles and vertical bars) derived from 2-D velocity field and model rotation curve (dashed) used to determine residuals in Figure 5. *Middle panel*: position angles at different radii and adopted position angle (dashed line). *Bottom panel*: the observed (circles and bars) and model (dashed curve) sums of systematic and off-plane components of the line-of-sight velocity in Arp 10.

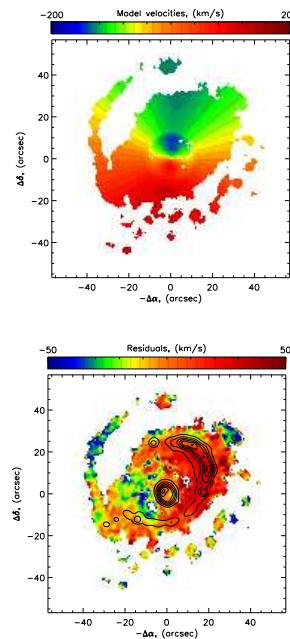


FIG. 7.— *Top panel*: the circular velocity field in Arp 10 constructed using equation (1) and values derived from the tilted-rings analysis. *Bottom panel*: Line-of-sight velocity residuals in Arp 10. A contour map of  $H\alpha$  emission is superimposed by thin black curves.

cal motions of ionized gas with an amplitude of the order of  $30 \text{ km s}^{-1}$ . The tilted-ring analysis performed for  $i = 22^\circ$  and  $V_r = 0$  also implies significant vertical velocities  $V_z$  in the vicinity of the inner ring (see middle and bottom panels in Figure 6).

2) The outer ring expands non-uniformly, with the ex-

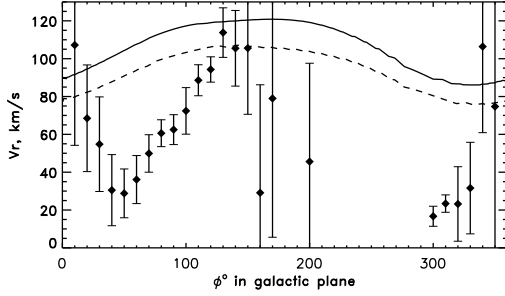


FIG. 8.— In-plane residual velocities (circles and error bars) at the outer ring of Arp 10 at different in-plane position angles  $\phi$  (which are counted from the south counterclockwise). The solid curve designates the model expansion velocities obtained in numerical simulations in § 8 at 85 Myr after the collision. The dashed curve is the same but for 105 Myr.

pansion velocity in the plane of the disk being larger in the North-Western part of the ring (top right in Figure 5) than in the South-Western part. Note that higher expansion velocities in the outer ring correspond to larger distances from the center. This implies that different parts of the outer ring has started to expand at the same time and from the same position in the disk, which favors the collisional origin of the outer ring in Arp 10.

The radial variations of the kinematic P.A. in the middle panel of Figure 6 is a distinctive feature of radial motions, according to Moiseev et al. (2004) and references therein. Note that we assume that all non-circular motions in the outer ring occur in the galactic plane and the azimuthal component of non-circular velocities is negligible. Strictly speaking, this is true only for the regions that lie at the minor axis (i.e. regions with P.A. =  $82^\circ$  and  $262^\circ$ ). In all other regions, the vertical and azimuthal components may contribute to the residuals.

The residual velocities in the inter-ring region may achieve rather high values. At the same time, the signal-to-noise ratio (S/N) is quite small there, which makes the interpretation of gas motions in the inter-ring region difficult.

To see how the expansion velocity in the plane of the disk  $V_r$  varies along the outer ring, we average  $V_r$  over 7 pixel ( $\sim 5$  arcsec) circular regions, which are regularly spaced along the ring. The resulting distribution of  $V_r$  along the outer ring is shown in Figure 8 as a function of angle  $\phi$ . Here  $\phi$  is measured counterclockwise in the plane of Arp 10 from its south direction. The fastest expanding part ( $\approx 110 \text{ km s}^{-1}$ ) of the outer ring at  $\phi \sim 130^\circ - 150^\circ$  corresponds to the highest surface brightness in  $H\alpha$ . The opposite side of the ring at  $\phi \sim 310 - 330^\circ$  expands considerably slower (up to  $30 \text{ km s}^{-1}$ ).

## 5. LONG-SLIT SPECTRA OF ARP 10

Although we obtained three long-slit radial cuts, only the second cut (hereafter, cut 2) is well suited for the analysis of emission and absorption lines because of its wide spectral coverage and best S/N ratio.

### 5.1. Emission lines

The most intensive emission lines are seen in the star-forming rings of Arp 10. Cut 2 in Figure 2 (P.A.= $118^\circ$ ) covers the regions of most intensive emission and ranges from  $3700 \text{ \AA}$  to  $7400 \text{ \AA}$ , which allows us to estimate extinction and heavy element abundances along the cut.

To estimate the extinction, we use the  $H\alpha/H\beta$  line ratio. For the correct extinction and abundance analysis, we have to take the absorption lines into account.

In order to obtain the emission line fluxes, we fit the observed spectrum around several selected spectral lines ([OII] $\lambda\lambda 3727, 3729$ ,  $H\beta$ , [OIII] $\lambda 4959$ , and [OIII] $\lambda 5007$ ) with a combination of model continuum, absorption lines, and one Gaussian emission line. In the case of blended lines ( $H\alpha$ , [NII] $\lambda 6548$ , [NII] $\lambda 6584$ ), three Gaussian emission lines were used. The free parameters were the width and height of emission lines, and the height of continuum. The best-fit parameters were used to obtain the emission line fluxes. These fluxes at different distances from the center of Arp 10 are given in Table 2.

The extinction in the V-band ( $A_V$ ) from HII regions located at different radii is estimated using the parameterization of Charlot & Fall (2000). The results are shown in Table 3. The extinction can be determined only in star-forming rings: it attains a mean value of 0.32 mag in the inner ring and increases toward the outer ring, reaching a maximum value of 4.0 mag in the external part of the outer ring. This is in general agreement with a propagating star formation scenario – massive young stars destroy dust and decrease extinction in the wake of a propagating wave of star formation. The observed emission fluxes in Table 2 were corrected for extinction and then were used to evaluate the oxygen abundance in Arp 10. The temperature-sensitive line [OIII] $\lambda 4363$  is not seen in our spectra. Instead, we follow an approach described by Pilyugin & Thuan (2005), which uses the excitation parameter  $P$  based on the [OII] $\lambda\lambda 3727, 3729$  to [OIII] $\lambda\lambda 4959, 5007$  relation  $R_{23}$ :

$$12 + \log(O/H) = \frac{R_{23} + 726.1 + 842.2P + 337.5P^2}{85.96 + 82.76P + 43.98P^2 + 1.793R_{23}}, \quad (2)$$

where  $P = R_3/(R_2 + R_3)$ ,  $R_2 = I_{[\text{OII}]\lambda\lambda 3727, 3729}/I_{H\beta}$ ,  $R_3 = I_{[\text{OIII}]\lambda\lambda 4959, 5007}/I_{H\beta}$ , and  $R_{23} = R_2 + R_3$ .

The derived abundance of oxygen will be applied in the spectral index modeling in § 6. The shape of absorption spectral lines depends on abundances of heavy elements. In turn, the emission line fluxes (and hence the extinction and abundances) depend on the subtracted absorption spectrum. To determine abundances and extinction, we use the following procedure. We estimate extinction/abundances from emission lines and use the resulting values to derive the model absorption spectrum. The resulting spectrum in turn is used to derive a new approximation for the emission line fluxes and, by implication, for extinction/abundances. This procedure is iterated until convergence.

The resulting values of  $P$  and oxygen abundances  $12 + \log(O/H)$  are given in Table 3. These values agree with a mean value of  $12 + \log(O/H) = 8.6$  estimated by Bransford et al. (1998) for two HII regions in the outer ring of Arp 10. However, when a method of evaluating oxygen abundances from Bransford et al. (1998) is applied to our emission line fluxes, the obtained oxygen abundances exceed the solar value at all radii. This is unlikely for Arp 10 due to its presumably low surface density nature (see § 8.1). We note that the radial oxygen abundance gradient in Arp 10 is very small, with a mean oxygen abundance of 8.55 and 8.64 in the inner

and outer rings, respectively. This implies a negligible radial metallicity gradient in young stars as well.

One of the products of our analysis is the radial distribution of extinction-corrected fluxes in  $H\alpha$  and  $H\beta$ , which are shown in Table 3. The  $H\alpha$  fluxes were corrected for [NII]-emission by deblending. We note that the [NII]/ $H\alpha$  flux ratio is remarkably constant along the radius of Arp 10. Table 3 indicates that  $[NII]\lambda 6584/H\alpha = 0.37 \pm 0.01$  and  $([NII]\lambda 6548 + [NII]\lambda 6584)/H\alpha = 0.48 \pm 0.05$ . These values are typical for quiescent regions in regular galaxies rather than for regions where strong shock waves are seen (Kennicutt & Kent 1983; Moiseev 2000). It suggests that propagating gas density waves in Arp 10 do not generate strong shock waves.

### 5.2. Spectral indices

The equivalent width of absorption lines in galaxies depends on a contribution of stellar populations of different ages. In case of Arp 10, we assume that stellar populations consist of old background stars and young stars. The latter were born after a passage of a star formation wave associated with an expanding gas density wave. We apply several population synthesis codes to construct model spectra and estimate the relative amount of old and young stars at a specific radius in Arp 10. The propagating wave of star formation in Arp 10 is approximated by a sequence of single-burst events. Spectra of single-burst populations are functions of age, metallicity, and initial mass function (IMF). We assume that the IMF has a universal nature and does not depend on a particular location in Arp 10.

In order to compare model and observed spectra, the latter should be corrected for internal extinction. The values of V-band extinction from HII regions estimated in § 5.1 may differ considerably from the interstellar extinction in other regions of Arp 10. Fortunately, most spectral indices do not depend on extinction, since they are defined in relatively narrow bands of the spectrum. We use index definitions by Worthey (1994), Worthey & Ottaviani (1997), Trager et al. (1998), and Gorgas et al. (1999). Out of 31 indices, 27 can be measured in our spectral range.

To find the indices that can effectively serve as indicators of age and metallicity, we use three population synthesis codes: STARBURST99 (the latest version is based on Vazquez & Leitherer 2005), GALAXEV (Bruzual & Charlot 2003), and Worthey's code (Worthey 1994). The STARBURST99 code produces high-resolution synthetic spectra with dispersion  $0.3 \text{ \AA pixel}^{-1}$  in our spectral range. It allows us to smooth the model spectra down to our resolution of  $5 \text{ \AA}$  and  $8 \text{ \AA}$ . The STARBURST99 code allows to obtain spectra of a single-burst population and to choose parameters for a given IMF. We use the Kroupa IMF (Kroupa 2001) and Padova set of stellar models. The spectral indices were calculated from the obtained high resolution synthetic spectra. The GALAXEV code provides spectral indices for a set of ages, metallicities, spectral resolutions, and stellar velocity dispersions. We choose the Chabrier IMF (Chabrier 2003), which is similar to the Kroupa IMF, and Padova evolutionary tracks. The third population synthesis code (Worthey 1994) is considered here only for illustrative purposes because of its incompleteness at ages of the order of 100 Myr.

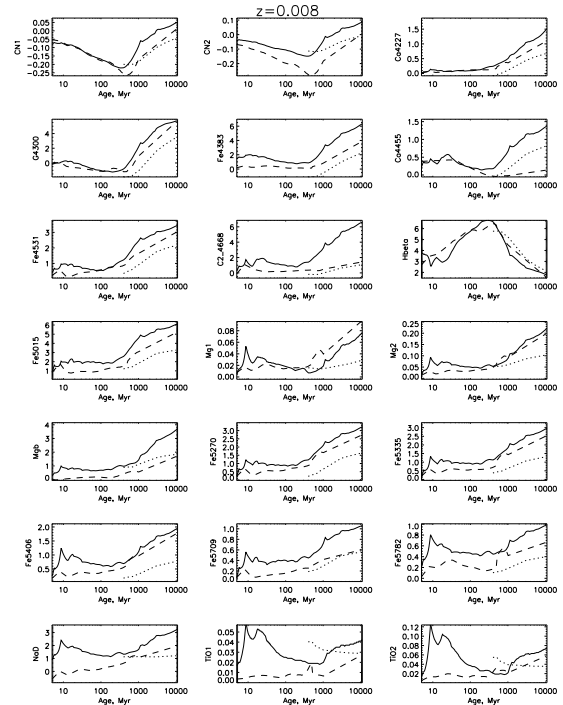


FIG. 9.— Eighteen spectral indices derived for a single-burst stellar population with metallicity  $z = 0.008$  (assuming that the solar metallicity is 0.02) at different ages in three models: solid curves – GALAXEV (Bruzual & Charlot 2003), dashed curves – STARBURST99 (Gonzalez Delgado et al. 1999), dotted curves – Worthey (Worthey 1994).

Figure 9 shows how the spectral indices obtained with STARBURST99 (dashed lines), GALAXEV (solid lines), and Worthey's code (dotted lines) change with age of a single-burst population. The metallicity is fixed in all models and equal to 0.008 (assuming 0.02 for the solar metallicity), which is close to a mean value of metallicity of young population derived for Arp 10 in § 5.1. We note that the indices derived with the Worthey's code do not extend below 400 Myr. STARBURST99 and GALAXEV show general agreement, although a systematic offset in the values of indices is seen between the two codes. For our analysis, we need spectral indices that show a significant monotonous variation with age. As is seen in Figure 9, not all indices change monotonously between 0 Myr and 500 Myr, which is an expected range of ages of young stars in collisional ring galaxies. Some indices vary negligibly with age. An additional uncertainty is introduced by a dependence of spectral indices on metallicity. In principle, the hydrogen line indices based on the strength of  $H\beta$ ,  $H\gamma$ , and  $H\delta$  lines are the best age indicators. Unfortunately, a presence of emission lines makes it impossible to utilize them. Another age-sensitive index  $D4000$  has to be used with caution, because it is defined on a  $500 \text{ \AA}$  bandpass in the blue part of spectrum and thus depends on the poorly known value of internal extinction. For instance, an extinction of  $A_V = 1 \text{ mag}$  will decrease  $D4000$  by 7% Gorgas et al. (1999). Three iron-sensitive indices (Fe5406, Fe5709, and Fe5782) are not good for the analysis, because their bandpasses interfere with strong night sky lines in our spectra. Finally, we accept 18 spectral indices for the further analysis of Arp 10. The observed radial distribution of these indices is shown in Figure 10

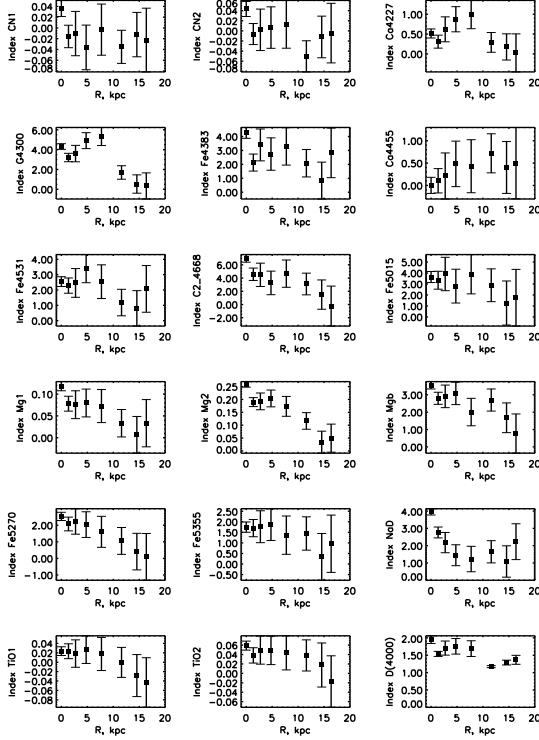


FIG. 10.— Eighteen spectral indices (the same as in Figure 9) observed in Arp 10 at different distances from the center for long-slit cut 2.

A brief inspection of Figure 10 and comparison of Figure 10 with Figure 9 show that the indices are sensitive to the presence of young stars in the inner and outer rings. Systematically smaller values of Fe, Mg, Ca, Ti, and D4000 indices are seen in the both rings. Since Arp 10 is unlikely to have a similar systematic variation in metallicity, the observed variation of indices should be interpreted as a presence of young stellar population.

## 6. SPECTRAL INDEX MODELING OF PROPAGATING STAR FORMATION IN ARP 10

In this section we make predictions about metallicities and ring propagation velocities in Arp 10 by fitting the radial distribution of model spectral indices to that of the observed ones.

### 6.1. Model description

We assume for simplicity that the stellar disk of Arp 10 consists of young and old stellar populations. The old stellar population has an age of either 10 Gyr or 5 Gyr. The former value is typical for elliptical galaxies without ongoing star formation and early-type spiral galaxies. The latter value is typical for blue low surface brightness and for late-type galaxies. These values are chosen to represent two limiting ages of old stellar populations in galaxies. The old stellar population in our model consists of an exponential disk and bulge, the radial scale lengths of which ( $h_{old} = 7.2$  kpc and  $h_b = 1.77$  kpc, respectively) were obtained from photometry in § 3. The radial surface density distribution of the old stellar population is described as

$$\Sigma^{old} = \Sigma_0^{old}(17.67 \exp(-r/h_b) + \exp(-r/h_{old})), \quad (3)$$

where  $\Sigma_0^{old}$  is derived in § 8 to be  $300 M_\odot \text{ pc}^{-2}$  and the bulge-to-disk ratio of their central surface densities

is 17.67.

The young population emerges after a passage of two circular gas density waves, which propagate from the center of Arp 10 toward its periphery and trigger star formation. We assume constant propagation velocities of the outer and inner waves (representing the outer and inner rings) and denote their values by  $V_{outer}$  and  $V_{inner}$ , respectively. We assume that the radial distribution of metallicity of both young and old stars can be approximated by a linear function of radius. In the following text, we normalize metallicities (derived from the spectral index modeling) to the solar value ( $z = 0.02$ ) and denote the resulting relative metallicities as  $Z$ . Using the oxygen abundance estimates in § 5.1 and assuming that the fractional abundances in Arp 10 are similar to those at the Sun, we assume the relative metallicity of young stars in the center of Arp 10 to be  $Z_{0,y} = -0.3$  dex. The metallicity gradient of young stars  $(dZ/dr)_y$  is negligible and we set its value to zero.

We find the metallicity of old stars  $Z_{0,old}$  in the center of Arp 10 and metallicity gradient  $(dZ/dr)_{old}$  using the least-square fit of model spectral indices to the observed indices in the inner 0.7 kpc and in the outer region between 16.3 kpc and 18.8 kpc. This can be done because the region outside the outer ring consists of the old stellar population only. The center of Arp 10 does contain a certain fraction of the young stellar population, but its contribution is expected to be small due to the presence of a high surface brightness bulge. First, we use all the indices shown in Figure 10, except for CN1, CN2, and NaD which were found to worsen the fit. This yields  $Z_{0,old} = -0.03 \pm 0.11$  dex and  $(dZ/dr)_{old} = -0.10 \pm 0.06$  dex  $\text{kpc}^{-1}$ . If we consider only Ca, Mg, and Ti-dominated indices, we obtain  $Z_{0,old} = 0.08 \pm 0.09$  dex and  $(dZ/dr)_{old} = -0.08 \pm 0.12$  dex  $\text{kpc}^{-1}$ . When the iron-dominated indices (G4300, Fe4383, Fe4531, and Fe5270) are considered, we found that  $Z_{0,old} = -0.35 \pm 0.06$  dex and  $(dZ/dr)_{old} = -0.08 \pm 0.02$  dex  $\text{kpc}^{-1}$ . The values of  $(dZ/dr)_{old}$  derived using different sets of indices are similar to each other, whereas the values of  $Z_{0,old}$  obtained from the iron- and  $\alpha$ -element dominated indices are significantly different. The values of the abundance gradients are typical for spiral galaxies (from -0.18 to 0.0, according to Zaritsky et al. 1994; van Zee et al. 1998; Rolleston et al. 2000).

We assume that the radial surface density distribution of young stars can be approximated by an exponential function  $\Sigma^y = \Sigma_0^y \exp(-r/h_y)$ . The central surface density of young stars  $\Sigma_0^y$  is expressed in term of the central surface density of gas  $\Sigma_0^g = \epsilon \Sigma_{g0}$ , where  $\Sigma_{g0} = 22 M_\odot \text{ pc}^{-2}$ . The coefficient  $\epsilon$  is a free parameter, which characterizes the gas to stars conversion efficiency and possible variation of the gas surface density. We denote  $h_y$  to be the radial scale length of young stars. The value of  $h_y$  is set to be equal or larger than the exponential scale length of the old stellar disk (7.2 kpc), since the gas disk usually has a shallower radial surface density profile than the stellar disk, particularly, in Arp 10 (Charmandaris & Appleton 1996).

We calculate the model spectral indices  $I_m$  as

$$I_m(r) = \frac{A_{old} + A_y}{C}, \quad (4)$$

if the index is defined in units of equivalent width

(Worthey 1994) or as

$$I_m(r) = -2.5 \log \frac{B_{\text{old}} + B_y}{C}, \quad (5)$$

if the index is measured in magnitudes. The coefficients  $C$ ,  $A_{\text{old},y}$ , and  $B_{\text{old},y}$  are determined as

$$\begin{aligned} A_{\text{old},y} &= \Sigma^{\text{old},y}(r) L_V(T_{\text{old},y}, Z_{\text{old},y}) \times \\ &\quad \times I_{\text{old},y}(T_{\text{old},y}, Z_{\text{old},y}), \\ B_{\text{old},y} &= \Sigma^{\text{old},y}(r) L_V(T_{\text{old},y}, Z_{\text{old},y}) \times \\ &\quad \times 10^{-0.4 I_{\text{old},y}(T_{\text{old},y}, Z_{\text{old},y})}, \\ C &= \Sigma^{\text{old}}(r) L_V(T_{\text{old}}, Z_{\text{old}}) + \\ &\quad + \Sigma^y(r) L_V(T_y, Z_y). \end{aligned} \quad (6)$$

The superscripts/subscripts “old” and “y” refer to old and young stellar populations, respectively. The V-band luminosity of a single-burst population with relative metallicity  $Z_{\text{old}}$  or  $Z_y$  and age  $T_{\text{old}}$  or  $T_y$  is denoted as  $L_V$ . Spectral indices of a single-burst stellar population are denoted as  $I$ .

Our model has four free parameters: the gas-to-star conversion efficiency  $\epsilon$ , scale length  $h_y$ ,  $V_{\text{outer}}$ , and  $V_{\text{inner}}$ . Chi-square values  $\chi^2$  are calculated for all selected indices using their model and observed values (along with their uncertainties) at different radii. An integrated value of  $\chi^2$  indices is found by summing the individual  $\chi^2$  indices. We determine the free parameters of our model by minimizing the integrated  $\chi^2$  value. We used the Levenberg-Marquardt optimization algorithm. The wave propagation velocities may be non-isotropic. Therefore, a best match between model and observed spectral indices was obtained separately for the lower-left and upper-right halves of cut 2 in Figure 2.

### 6.2. Results of spectral modeling

A comparison of Figures 9 and 10 indicates that synthetic spectral indices obtained with STARBURST99 often fall outside the range covered by the observed indices. This effect does not depend on the S/N ratio of the spectra or uncertainty in the indices. One of the most prominent examples of this discrepancy is seen for Mg b: no agreement between the model and observations can be achieved for any parameters of stellar populations. At the same time, the model and observed radial distributions of the Mg b index are nearly parallel to each other. We find that synthetic indices obtained with GALAXEV reproduce the range covered by observed indices better than STARBURST99. Therefore, we use the GALAXEV code to obtain synthetic indices in this paper.

First, we consider fifteen observed spectral indices shown in Figure 10. The best match between these indices and model indices is achieved for the following values of free parameters:  $V_{\text{outer}} = 180_{-55}^{+215}$  km s<sup>-1</sup>,  $V_{\text{inner}} = 46_{-15}^{+45}$  km s<sup>-1</sup>,  $h_y = 14$  kpc. Although the uncertainty in the propagation velocity of the outer ring is rather large, the value of  $V_{\text{outer}}$  suggest a very fast expansion of the outer ring. The radial distributions of the model (open diamonds) and observed (filled squares with error bars) indices obtained along the upper half of cut 2 are shown in Figure 11.

Second, we consider the spectral index D4000 alone. Although the D4000 index may be affected by an poorly

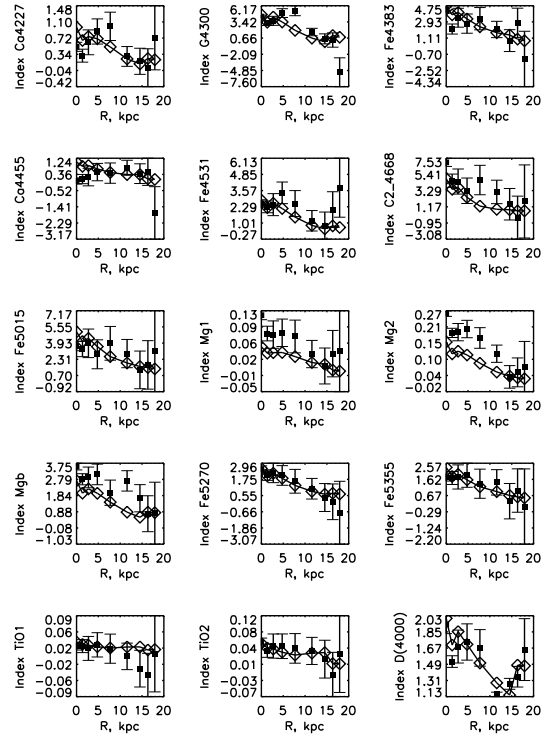


FIG. 11.— Fifteen model (solid curve and open diamonds) and observed (filled squares and error-bars) spectral indices at different distances from the center of Arp 10.

known value of internal extinction, mean gas surface density (see § 8) implies a rather small mean value of  $A_V = 0.2$  mag (Bohlin et al 1978). This value of extinction may decrease the D4000 index by only 1.5%. The best match between the observed and model D4000 indices is obtained for the following values:  $V_{\text{outer}} = 180_{-50}^{+365}$  km s<sup>-1</sup>,  $V_{\text{inner}} = 58_{-12}^{+16}$  km s<sup>-1</sup>, and  $h_y = 65$  kpc. Finally, we consider two more combinations of spectral indices: Ca, Mg, Ti, D4000 and Fe, D4000. The resulting free parameters also suggest a large expansion velocity for the outer ring and large value of  $h_y$ .

The free parameter  $\epsilon$  takes a best-fit value of approximately 0.4. This value is a factor of four larger than a typical efficiency of gas-to-stars conversion in star-forming regions. A larger value of  $\epsilon$  suggests that either the surface density of gas is larger than it was assumed and/or the efficiency of star formation is higher. A higher star formation efficiency was indeed reported for the Cartwheel ring galaxy by Vorobyov (2003). The above spectral modeling assumed that the old stellar population had a mean age of 5 Gyr. A larger value of 10 Gyr yields only a slightly worse agreement between the model and observed indices.

## 7. THE INTRUDER GALAXY

One of the candidates for the intruder galaxy was investigated by Charmandaris & Appleton (1996). They found that a companion located 60 arcsec North-East of the main galaxy is a distant background galaxy. They also suspected another candidate for the intruder galaxy which can be seen as a small “knot” 5 arcsec to the South-West of the nucleus of Arp 10. We consider this possibility and make our third long-slit cut through this object (hereafter, the companion). The companion has a typical

galactic spectrum with absorption Balmer lines.

The radial velocity of the companion exceeds the systematic velocity of Arp 10 by  $480 \text{ km s}^{-1}$ . The position-velocity diagram made with the help of absorption lines in a wavelength band from  $5000 \text{ \AA}$  to  $5400 \text{ \AA}$  is shown in Figure 12. The line-of-sight velocity distribution was obtained via a cross-correlation of the object spectra against a twilight-sky template observed at the same night. It is clearly seen that the companion has a noticeable velocity dispersion  $240 \text{ km s}^{-1}$ , which is comparable to that of Arp 10. We consider isodensities that outline both Arp 10 and companion in Figure 12 and estimate a maximum range of distances  $\Delta r$  and velocities  $\Delta V$  covered by these isodensities for Arp 10 and companion. The kinematic masses of Arp 10 and companion are then estimated using the following formula  $M = \Delta V^2 \Delta r / G$ . The resulting target-to-companion mass ratio is about 4, which corresponds to the total mass of companion about  $2 \times 10^{11} M_{\odot}$ . Of course, only the inner part of Arp 10 was included in the analysis. Arp 10 appears to be much more extended than the companion, yet the faint parts of the latter might be difficult to observe.

We note that the target-to-companion mass ratio can be larger if the companion is a non-virialized stellar system. On the other hand, the companion may lose a substantial part of its mass during the collision (about  $1/3$  in a model of Lynds & Toomre 1976), hence the pre-collision mass of the companion can be larger.

Our B-, R-band and  $H\alpha$  images of Arp 10 do not resolve the structure of the companion's outer regions. Nevertheless, indirect evidence of the companion type comes from the position-velocity diagram in Figure 12, our  $H\alpha$  image, and HI map of Charmandaris & Appleton (1996). Neither significant amount of HI nor ionized gas are seen in the region of the "knot". At the same time, the stellar velocity dispersion is quite large and the companion appears to be compact. A visual inspection of Figure 12 indicates that the companion has a size of 5 arcsec or 3 kpc. This suggests that the companion is located behind the galactic plane of Arp 10 and is shielded by the disk of the main galaxy.

We consider several possibilities for the type of the companion, which might have been a disk, elliptic, or irregular galaxy before the collision. Disk galaxies are expected to contain a modest amount gas, which might have been stripped off after the collision. Indeed, a gas condensation can be seen in the HI map of Arp 10 published by Charmandaris & Appleton (1996) (see their figure 4, top left panel and figure 5). A relatively high line-of-sight velocity of this gas clump suggests that it may not belong to Arp 10. The location of the clump does not coincide exactly with the companion's nucleus, as is indeed expected if the companion is not traveling along the line of sight.

A large total mass of the companion and regular shapes of its isophotes argue against a supposition that the companion was an irregular galaxy before the collision. The characteristic age of about 5 Gyr for the companion's stellar population (see § 7.1) implies that the companion was a spiral rather than an elliptical galaxy.

#### 7.1. Constraints on the companion's age from its spectrum

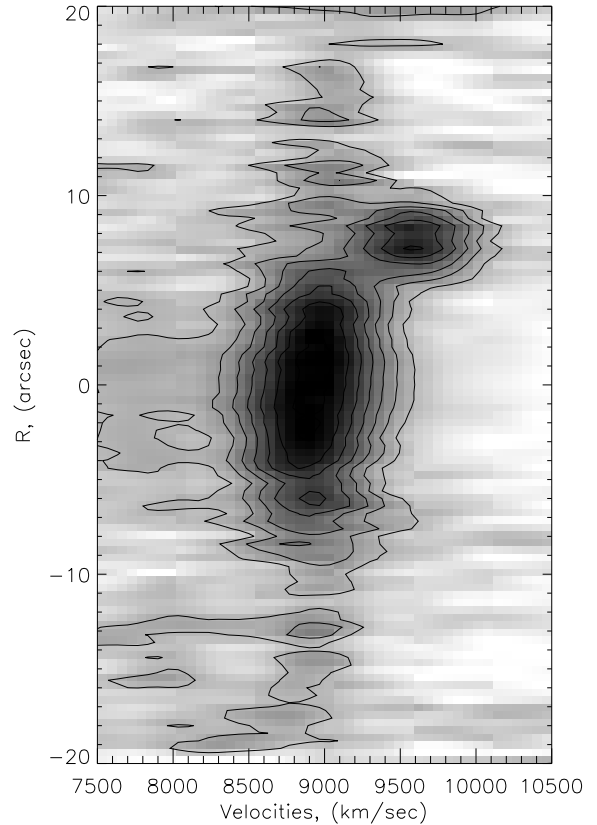


FIG. 12.— Position-Velocity diagram for stellar line-of-sight velocity distribution (grey-scale) and contour map for the central 20 arcsec in Arp 10. A difference in the radial velocities of Arp 10 and companion is approximately  $480 \text{ km s}^{-1}$ .

The spectrum of the companion shows no emission lines. This allows us to use the  $H\beta$ ,  $H\gamma$ , and  $H\delta$  spectral indices to estimate the mean age of stellar population in the companion. In Figure 13 we show  $H\beta$  versus  $Mg\ b$  (upper panel) and  $H\beta$  versus  $Mg\ 2$  (lower panel) relations obtained from single-burst models with different ages and metallicities. The model indices were obtained using the GALAXEV package (Bruzual & Charlot 2003) and adopted to our spectral resolution and velocity dispersion. The dotted lines in Figure 13 connect the indices with equal metallicities of 0.008, 0.001, and 0.0008. The indices with a solar metallicity  $z = 0.02$  are connected by the dash-dotted line. On the other hand, the indices with equal ages of 0.4 Gyr, 2 Gyr, 3 Gyr, and 5 Gyr are connected by the dashed lines. The solid line with squares connects the indices with an age of 10 Gyr.

The observed indices of the companion are shown by the filled diamonds with the error bars in each panel of Figure 13. As can be seen, a single-burst model with an age of 5 Gyr and metallicity  $z = 0.008$  yields model indices that are similar to those of the companion. An estimated mean age of 5 Gyr for the companion's stellar population implies that the companion was a spiral rather than an elliptical galaxy.

Now, we model the  $H\beta$  spectral index under an assumption of continuous star formation. More specifically, we assume that the star formation rate declines exponentially with time as  $SFR \sim \exp(-\beta \cdot t)$ , where  $1/\beta$  is the characteristic time scale for star formation. In elliptical galaxies  $1/\beta$  is less than 1 Gyr (Sandage 1986), whereas

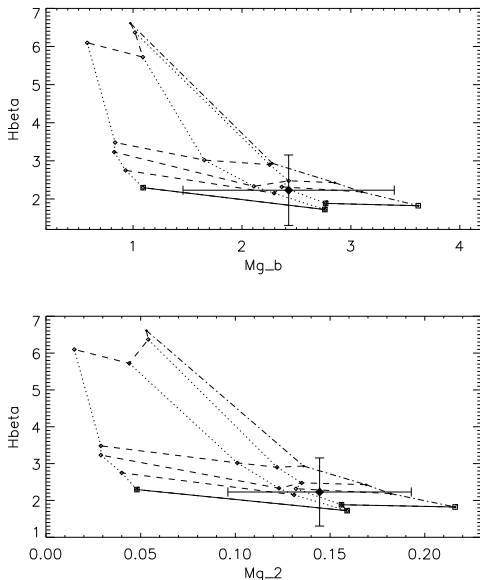


FIG. 13.—  $H\beta$  versus  $Mg_2$  (top) and  $H\beta$  versus  $Mg_b$  (bottom) diagrams. Observed spectral indices of the companion are designated by filled diamond with error bars. The dotted lines connect spectral indices of a single-burst populations with equal metallicities of 0.008, 0.001, and 0.0008. The indices for the solar metallicity  $z = 0.02$  are connected by the dash-dotted line. Spectral indices of the single-burst populations with equal ages of 0.4 Gyr, 2 Gyr, 3 Gyr, and 5 Gyr are connected by the dashed lines. The solid line with squares connects the indices for the age of 10 Gyr.

$1/\beta \rightarrow \infty$  in irregular systems (Gallagher et al. 1984). The resulting  $H\beta$  spectral index is

$$I_{H\beta} = \int_0^T I(t, z) L_V(t, z) SFR dt, \quad (7)$$

where  $I(t, z)$  is the value of the  $H\beta$  index for a single-burst stellar population with age  $t$  and metallicity  $z$ ,  $V$ -band luminosity  $L_V$  is the same as in equation (6), and  $T=15$  Gyr. For the estimated metallicity of the companion  $z = 0.008$ , the observed value  $H\beta = 2.25 \text{ \AA}$  corresponds to  $1/\beta \approx 4$  Gyrs, which is typical for Sab galaxies (McGaugh & de Blok 1997).

The foreground young population of Arp 10 and possible (yet undetected) Balmer line emission from the companion may change the values of Balmer indices. This may alter the obtained values of mean age and characteristic time scale for star formation in the companion. However, this effect is expected to be small due to a lack of gas in the companion. Moreover, the emission-independent indices  $Mg_b$  and  $Mg_2$  in Figure 13 suggest a similar mean age of the companion.

### 7.2. Synchronized motion of the outer ring and companion

The companion has a very high velocity of  $480 \text{ km s}^{-1}$  relative to Arp 10. A mean rotation velocity of Arp 10 is about  $300 \text{ km s}^{-1}$  (see Fig. 6), which implies that the escape velocity for Arp 10 is about  $420 \text{ km s}^{-1}$  and the companion may not be gravitationally bound. However, a near-central collision suggests that Arp 10 may have a massive dark matter halo that extends far beyond 50 arcsec. In this case, the companion would be marginally bound to Arp 10. This might also allow for a much earlier encounter that might have generated the faint ripples

noted by Charmandaris & Appleton (1996). The numerical modeling in § 8 indicates that approximately 85 Myr has passed since the collision and the current distance to the companion from the center of Arp 10 is about 50 kpc. At the same time, the projected distance from the companion to the center of inner ring of Arp 10 is about 3 kpc. Hence, the direction of the companion motion after the collision nearly coincides with the line of sight.

The numerical modeling in § 8 suggests that the companion might have changed significantly its direction of motion after the encounter. Position angles of the companion and the brightest part of the outer ring are different. The rotation curve of Arp 10 indicates that it takes approximately 170 Myr for the brightest part of the outer ring to complete a circle. This implies that the ring has made about half a turn since its emergence 85 Myr ago. We reconstruct a synchronized motion of the companion and outer ring as follows. The companion passed through the disk of Arp 10 about 3 kpc to the South-East from the nucleus and generated an expanding asymmetric density wave in the disk of Arp 10. The position of maximum density perturbation was initially in the South-Eastern part of Arp 10 but later relocated to the North-Western part due to rotation. The companion is now seen 3 kpc to the South-West of the nucleus.

## 8. NUMERICAL MODELING OF ARP 10

In this section we perform a simplified two-dimensional hydrodynamic modeling of ARP 10. We want to see if the collision with a likely intruder galaxy can reproduce the observed sizes of the inner and outer rings and expansion velocity of the outer ring. We assume that the rings of ARP 10 are a manifestation of gaseous (rather than stellar) density waves that propagate in the gas disk of the galaxy. This conjecture is motivated by the fact that most disk galaxies have their gas disks extending far beyond stellar disks. The spectral modeling in § 6.2 suggests that the radial scale length of the stellar disk in Arp 10 ( $\approx 7.2$  kpc) is much smaller than that of the gas disk. A neutral hydrogen imaging of Arp 10 by Charmandaris & Appleton (1996) also shows that the gas disk extends at least 2.7 times the mean size of the outer ring. Therefore, we neglect density perturbations in the stellar component of Arp 10 and assume that the stellar disk serves merely as a source of axisymmetric gravitational potential.

### 8.1. Model description and basic equations

Our model galaxy consists of a thin self-gravitating gas disk, which evolves in the combined gravitational potential of a spherical dark matter halo, spherical bulge, thin stellar disk, and companion galaxy. The gas disk is assumed to be isothermal at  $T = 9000 \text{ K}$ . We use the thin-disk approximation to describe the motion of gas in Arp 10. In this approximation, the radial extent of the gas disk is assumed to be much larger than its vertical height, discarding the need to solve for the vertical motion of gas. A near-vertical impact may send ripples through the gas disk of a target galaxy. We assume that these vertical oscillations have little effect on the appearance of Arp 10 due to its low inclination.

The basic equations governing the dynamics of the gas

disk in Arp 10 are

$$\frac{\partial \Sigma_g}{\partial t} = -\nabla \cdot (\mathbf{v} \Sigma_g), \quad (8)$$

$$\frac{\partial \mathbf{v}}{\partial t} + (\mathbf{v} \cdot \nabla) \mathbf{v} = -\nabla \Phi_g - \nabla \Phi_{s,b,h,i} - \frac{\nabla P}{\Sigma_g}. \quad (9)$$

Here,  $\Sigma_g$  is the gas surface density,  $\mathbf{v}$  is the gas velocity in the disk plane,  $P = c_s^2 \Sigma_g$  is the vertically integrated gas pressure, and  $c_s$  is the sound speed. The gravitational potentials of the gas disk  $\Phi_g$ , bulge  $\Phi_b$ , stellar disk  $\Phi_s$ , dark matter halo  $\Phi_h$ , and companion  $\Phi_i$  are provided below.

In order to compute  $\Phi_g$ ,  $\Phi_b$ ,  $\Phi_s$ , and  $\Phi_h$ , we have to make assumptions about the total masses and radial profiles of gas, stars, and dark matter in Arp 10. The total atomic hydrogen mass in Arp 10 is  $1.1 \times 10^{10} M_\odot$  (Charmandaris & Appleton 1996, corrected for a distance of 130 Mpc). Hence, we set the total gas mass (atomic hydrogen plus helium) within a 50 kpc radius to be  $1.4 \times 10^{10} M_\odot$ . We neglect a possible contribution of molecular hydrogen because its mass is highly uncertain. The radial distribution of gas in the pre-collision Arp 10 is difficult to constrain. We assumed that the gas distribution in the pre-collision ARP 10 exponentially declined with radius and tried different values for the central gas surface density  $\Sigma_{g0}$  and exponential scale length  $r_{g0}$ . We found that the Toomre  $Q$ -parameter is larger or equal 2.0 throughout the disk irrespective of  $\Sigma_{g0}$  and  $r_{g0}$ . The  $Q$ -parameter may decrease below 2.0 only if  $r_{g0}$  is much smaller than the exponential scale length of the stellar disk  $h_{old} = 7.2$  kpc and the gas disk in the pre-collision Arp 10 was strongly concentrated to its center. The latter is unlikely because gas disks usually extend further in radius than stellar disks (see Charmandaris & Appleton 1996, for the case of Arp 10) and thus have shallower radial profiles. This implies that the pre-collision Arp 10 might have depleted its gas content and reached a tentative state of gravitational stability (see e.g. Zasov & Bizyaev 1996). We note that high values of the  $Q$ -parameter are typical for gas disks in low surface brightness galaxies. For our simulations we adopt  $r_{g0} = 12$  kpc and  $\Sigma_{g0} = 22 M_\odot \text{ pc}^2$ . We find that these values reproduce best both the radial and azimuthal distributions of H $\alpha$  surface brightness in Arp 10. The gravitational potential of a thin gas disk is then calculated by (Binney & Tremaine, Sect. 2.8)

$$\Phi_g(r, \phi) = -G \int_0^\infty r' dr' \times \int_0^{2\pi} \frac{\Sigma(r', \phi') d\phi'}{\sqrt{r'^2 + r^2 - 2rr' \cos(\phi' - \phi)}}. \quad (10)$$

This sum is calculated using a FFT technique which applies the 2D Fourier convolution theorem for polar coordinates.

The present-day rotation curve of Arp 10 is used to set constraints on the total masses of stellar and dark matter components. The Arp 10 rotation curve flattens at a radius of approximately 3 kpc and slowly rises at larger radii. We use a steady-state equation of motion for the azimuthal component of the gas velocity to fit the model

and measured rotation curves. We assume that the thin stellar disk of Arp 10 has an exponentially declining surface density profile, whereas the spherical bulge of Arp 10 has an exponentially declining volume density profile. The exponential scale lengths of the bulge  $h_b = 1.77$  kpc and stellar disk  $h_{old} = 7.2$  kpc are known from the R-band photometry of § 3. For the dark matter distribution we adopt a modified isothermal sphere

$$\rho_h = \frac{\rho_{h0}}{(1 + r/r_h)^2}, \quad (11)$$

where  $\rho_{h0}$  and  $r_h$  are the central volume density and characteristic scale length of the dark matter halo. The central densities of the stellar disk  $\Sigma_0^{old}$  and the bulge  $\rho_{b0}$ , and the dark matter halo profile are free parameters.

We find that the stellar disk and bulge (if considered alone) produce a declining rotation curve at radii larger than 10 kpc and hence cannot account for the shape of the rotation curve in Arp 10, irrespective of the total stellar mass. This means that Arp 10 must possess a massive dark matter halo. The exact mass partition between different components is somewhat uncertain. In fact, a strongly concentrated dark matter halo can approximately reproduce the Arp 10 rotation curve without invoking the need for the stellar disk or bulge. However, it would contradict the presence of a considerable old stellar population in Arp 10 as implied by spectral modeling in § 6.2. After experimenting with different values of the free parameters, we find that the rotation velocity of Arp 10 at large radii ( $\approx 320 \text{ km s}^{-1}$ ) is best reproduced by a massive halo with  $M_h = 8 \times 10^{11} M_\odot$ ,  $r_h = 1.5$  kpc, and  $\rho_{h0} = 0.6 M_\odot \text{ pc}^{-3}$ . We also include a stellar disk and bulge with masses and central densities  $M_s = 1.0 \times 10^{11} M_\odot$ ,  $\Sigma_0^{old} = 300 M_\odot \text{ pc}^{-2}$  and  $M_b = 4 \times 10^{10} M_\odot$ ,  $\rho_{b0} = 0.3 M_\odot \text{ pc}^{-3}$ , respectively. All masses are calculated within a 50 kpc radius of Arp 10. The masses of the stellar disk and bulge are in fact the upper limits, because a more massive stellar disk and bulge would generate a declining rotation curve at radii larger than 15 kpc, which apparently contradicts the slowly rising rotation curve of Arp 10. We note that the parameters of the stellar disk (see Bizyaev et al. 2002; Bizyaev & Kajsın 2004), when taken together with high values of the  $Q$ -parameter, strongly suggest a low surface brightness nature of the pre-collision Arp 10. It is not unexpected that interacting (colliding) galaxies may have had low surface brightness progenitors. This is because interactions usually produce a new specific structure, which is much easier to see if the progenitor galaxies have been of low surface brightness. Otherwise, the new structure may wash out unless the interaction is very strong. The detection of a low surface brightness progenitor of the interacting galaxy Arp 82 (Hancock et al. 2007) adds more credit to this hypothesis.

The model rotation curve (solid line), radial distribution of the  $Q$ -parameter (dashed line) in the pre-collision Arp 10, and the measured rotation curve (filled circles) of the present-day Arp 10 are shown in Figure 14. The model rotation curve shows good agreement with the measured curve except for the inner 3 kpc, where the measured curve rises steeper than the model one. We assume that the steep rise is probably caused by material that flows into the inner ring from the inter-ring region. Such a radial inflow of gas can indeed be seen in the

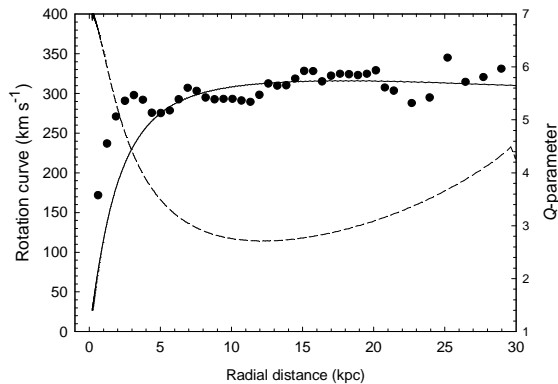


FIG. 14.— Model rotation curve (solid line) that is assumed in hydrodynamic simulations, radial distribution of the Toomre  $Q$ -parameter (dashed line), and observed rotation curve of Arp 10 (filled circles).

model velocity field obtained in the next section. Hence, the steep rise of the measured rotation curve could be a manifestation of angular momentum conservation and the pre-collision Arp 10 might have had no peak at 3 kpc and shallower rotation curve in the central region.

Once the parameters of the stellar disk, bulge, and the dark matter halo are determined, we can calculate their gravitational potentials. The gravitational potential of a thin stellar disk in the plane of the disk, the surface density of which declines exponentially with radius, can be evaluated as (Binney & Tremaine 1987)

$$\Phi_s = -\pi G \Sigma_0^{\text{old}} r [I_0(y) K_1(y) - I_1(y) K_0(y)], \quad (12)$$

where  $y = r/(2h_{\text{old}})$  and  $I_n$  and  $K_n$  are the modified Bessel functions of the first and second kinds. The radial gravity force per unit mass of a spherical bulge is evaluated as

$$\frac{\partial \Phi_b}{\partial r} = \frac{GM_b(r)}{r^2}, \quad (13)$$

where  $M_b(r)$  is the mass of the bulge contained within radius  $r$ . The radial gravity force per unit mass of a spherical dark matter can be written as

$$\frac{\partial \Phi_h}{\partial r} = 4\pi G \rho_{h0} r_h [r/r_h - \arctan(r/r_h)] \left(\frac{r_h}{r}\right)^2. \quad (14)$$

The companion is modeled as a point object with mass  $M_c = 2 \times 10^{11} M_\odot$  (see § 7), which moves in the combined gravitational potential of the dark matter halo and bulge. The equation of motion for the companion is solved using the forth-order Runge-Kutta method with adaptive step size control. The gravitational potential of the companion  $\Phi_i$  is calculated using a softened point-mass potential as described in Binney & Tremaine (1987), sect. 2.8. The softening parameter is set to 5 kpc.

### 8.2. Code description

An Eulerian finite-difference code is used to solve equations (8)-(9) in polar coordinates  $(r, \phi)$ . The basic algorithm of the code is similar to that of the ZEUS code presented by Stone & Norman (1992). The operator splitting is utilized to advance in time the dependent variables in two coordinate directions. The advection is treated using the consistent transport method of Stone and Norman and the van Leer interpolation scheme. The timestep is determined according to the usual Courant-Friedrichs-Lewy criterion. The numerical

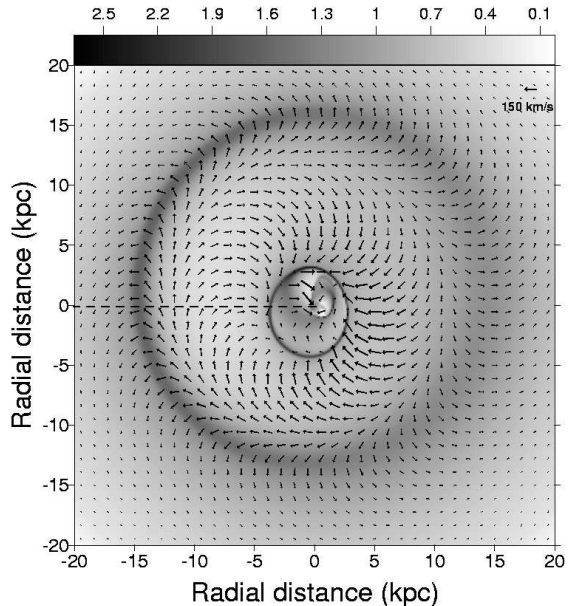


FIG. 15.— Model residual velocity field superimposed on the gas surface density distribution at  $t = 85$  Myr after the collision. The velocity of  $150 \text{ km s}^{-1}$  is indicated in the upper-right corner and scale bar on the top is in  $M_\odot \text{ pc}^{-2}$ . The dashed line shows the radial cut along which the circular velocity of gas is determined.

grid has  $512 \times 512$  points, which are uniformly spaced in the azimuthal direction and logarithmically spaced in the radial direction, i.e., the radial grid points are chosen to lie between the inner boundary  $r_{\text{in}} = 0.2$  kpc and outer boundary  $r_{\text{out}} = 50$  kpc so that they are uniformly spaced in  $\log r$ .

### 8.3. Results of numerical modeling

We model the collision by releasing the companion at 50 kpc above the disk plane of Arp 10. The initial velocity of the companion is  $490 \text{ km s}^{-1}$ . It falls near axially and hits Arp 10 at a distance of approximately 2.7 kpc from the center. At the time of impact, the companion velocity relative to Arp 10 is approximately  $800 \text{ km s}^{-1}$ . The gravitational perturbation from the companion sets off expanding density waves in the gas disk of Arp 10. Figure 15 shows the residual velocity field superimposed on the map of the gas surface density in Arp 10 at  $t \approx 85$  Myr after the collision. The residual velocity field is obtained by subtracting the circular velocities from the proper velocities of gas. Since we were limited by the two-dimensional approach, we could not fine-tune the numerical model to reproduce the exact visual appearance of Arp 10. Nevertheless, we were able to match the mean radii of the inner and outer rings,  $\approx 3$  kpc and  $\approx 14$  kpc, respectively. An overall expansion of the outer ring is clearly seen. The model radial expansion velocity of the outer ring as a function of azimuth at  $t = 85$  Myr is shown by the solid line in Figure 8. The maximum expansion velocity is approximately  $120 \text{ km s}^{-1}$ , which is in good agreement with a measured maximum expansion velocity of  $110 \pm 10 \text{ km s}^{-1}$ .

The flow of gas in the vicinity of the inner ring is complicated. The gas appears to stream toward the inner ring from the inter-ring region of Arp 10. This inward streaming motion of gas provides an extra compression to the inner ring, the gas surface density of which becomes an order of magnitude higher than that of the outer ring.

If outwardly propagating gas density waves are *axisymmetric*, then they can be identified by characteristic signatures in the azimuthal flow of gas in a galactic disk. Indeed, as the wave propagates outward, it pools the matter from both sides of the wave toward its current location. This should alter the circular velocity of gas  $V_\phi$  on both sides of the wave due to conservation of angular momentum. More specifically, the angular velocity of gas that lies ahead of the wave should increase, whereas the angular velocity of gas that lies behind the wave should decrease. Of course, any considerable deviation from axial symmetry of the wave would break the conservation of angular momentum. Nevertheless, these characteristic signatures can be detected in the radial distribution of  $V_\phi$ , if the latter is constructed along a narrow radial cut rather than being azimuthally averaged. Filled circles in Figure 16 show the radial distribution of  $V_\phi$  obtained along the upper half of cut 2 in Fig 2. A characteristic double-peaked shape is conspicuous. The outer and inner rings are located at approximately 15 kpc and 3 kpc, respectively. It is seen that  $V_\phi$  is growing across the outer ring from 11 kpc to 18 kpc, exactly as predicted from conservation of angular momentum of gas that is pooled toward the ring. The radial profile of  $V_\phi$  has a local minimum at 11 kpc, a radius at which the flow of gas is reversed from expansion to contraction toward the inner ring (see Figure 15). As a result,  $V_\phi$  starts to grow again at smaller radii and reaches a maximum near the position of the inner ring. Inside the inner ring,  $V_\phi$  quickly drops to a minimum. Similar double-peak radial profiles of  $V_\phi$  were found along the radial cuts taken at  $\pm 10^\circ$  and  $\pm 20^\circ$  away from cut 2. We note that the rotation curve in Figure 6 does not have a well-defined double-peaked shape, probably due to azimuthal averaging along circular rings. We compare the measured radial profile of  $V_\phi$  with that obtained in our numerical modeling. That is, we take a radial cut through the densest region in the outer ring (dashed line in Figure 15) and plot the resulting radial profile of  $V_\phi$  along this cut by the solid line in Figure 15. Although a quantitative agreement is difficult to attain in our simplified thin-disk model due to neglected vertical dynamics of Arp 10, a qualitative agreement is clearly seen and is encouraging. We consider a characteristic double-peak radial profile of circular velocity to be powerful evidence in favor of the collisional origin of Arp 10.

A good agreement between the modeled and measured sizes and maximum expansion velocities of the rings in Arp 10 suggests that approximately 85 Myr have passed since the collision. Our simulations indicate that the velocity of the companion has dropped to approximately  $480 \text{ km s}^{-1}$  at  $t = 85 \text{ Myr}$  after the collision, which is also in agreement with the measured velocity of the companion. The first resonant ring forms soon after the collision so that the age of the outer ring should be equal or less than 85 Myr. The spectroscopic analysis in § 6 suggests a similar age, 90 Myr.

The distribution of  $\text{H}\alpha$  emission from the outer ring of Arp 10 is characterized by a crescent shape (Figure 2). We test a conclusion of Charmandaris et al. (1993) that this peculiar  $\text{H}\alpha$  morphology is a result of both the off-center collision and star formation threshold in the gas disk of Arp 10. We model the  $\text{H}\alpha$  surface brightness in Arp 10 using a method described in Vorobyov (2003).

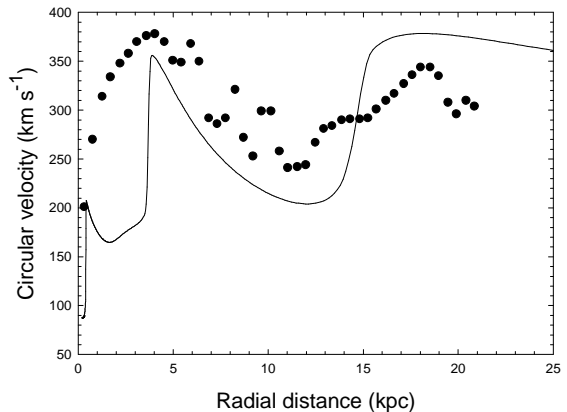


FIG. 16.— Comparison of radial distribution of the model circular velocities obtained along the radial cut in Figure 15 (solid line) with radial distribution of observed circular velocities along the upper half of radial cut 2 in Figure 2 (filled circles).

The star formation rate is assumed to obey a Schmidt law (Kennicutt 1998) in the form

$$\Sigma_{\text{SFR}} = 2.5 \times 10^{-4} \Sigma_{\text{g}}^{1.5}, \quad (15)$$

where the star formation rate  $\Sigma_{\text{SFR}}$  and gas surface density  $\Sigma_{\text{gas}}$  are measured in units of  $M_\odot \text{ yr}^{-1} \text{ kpc}^{-2}$  and  $M_\odot \text{ pc}^{-2}$ , respectively. We modify the Schmidt law (15) by assuming that star formation terminates if the Toomre  $Q$ -parameter exceeds  $Q_{\text{cr}} = 1.6$ , a critical value for stability of gas disks (characterized by a flat rotation curve) against local non-axisymmetric perturbations (Polyachenko et al. 1997). The star formation rate is converted to the  $\text{H}\alpha$  luminosity using a calibration of Kennicutt (1983) for solar metallicity

$$\text{SFR} (M_\odot \text{ yr}^{-1}) = 7.9 \times 10^{-42} L_{\text{H}\alpha} (\text{erg s}^{-1}). \quad (16)$$

Metal-poor stars produce more ionizing photons than metal-rich stars. The star-forming regions in Arp 10 have lower than the solar metallicity and equation (16) is expected to give a lower limit on the  $\text{H}\alpha$  luminosity. The extinction in the gas disk of Arp 10 is taken into account by estimating  $A_v$  from the model's known gas surface density via the relation given in Bohlin et al (1978) for  $R_v = 3.1$ . The model  $\text{H}\alpha$  fluxes are then corrected for the internal extinction  $A_{\text{H}\alpha} = 0.75 A_v$  (Cardelli et al. 1989).

Figure 17 shows the gas surface density distribution (left) and  $\text{H}\alpha$  surface brightness distribution (right) at three consecutive times after the collision  $t = 45 \text{ Myr}$ ,  $85 \text{ Myr}$ , and  $105 \text{ Myr}$ . The azimuthal distribution of  $\text{H}\alpha$  surface brightness in the outer ring has a characteristic crescent shape. The values of model  $\text{H}\alpha$  surface brightness  $\Sigma_{\text{H}\alpha}$  in the outer ring agree approximately with the values measured by Charmandaris et al. (1993). More specifically, the measured variation of  $\Sigma_{\text{H}\alpha}$  is between  $1.1 \times 10^{-16} \text{ erg s}^{-1} \text{ cm}^{-2} \text{ arcsec}^{-2}$  for the faintest part of the outer ring and  $6.7 \times 10^{-16} \text{ erg s}^{-1} \text{ cm}^{-2} \text{ arcsec}^{-2}$  for its brightest part. These values are not corrected for the internal extinction. The model predicts values equal or less than  $2 \times 10^{-16} \text{ erg s}^{-1} \text{ cm}^{-2} \text{ arcsec}^{-2}$  but corrected for the mean internal extinction in the outer ring  $A_{\text{H}\alpha} \approx 1.3 \text{ mag}$  as described above.

Comparison between  $\text{H}\alpha$  and gas distributions clearly indicates that the  $\text{H}\alpha$  emission originates from regions with the highest gas surface density. These regions are

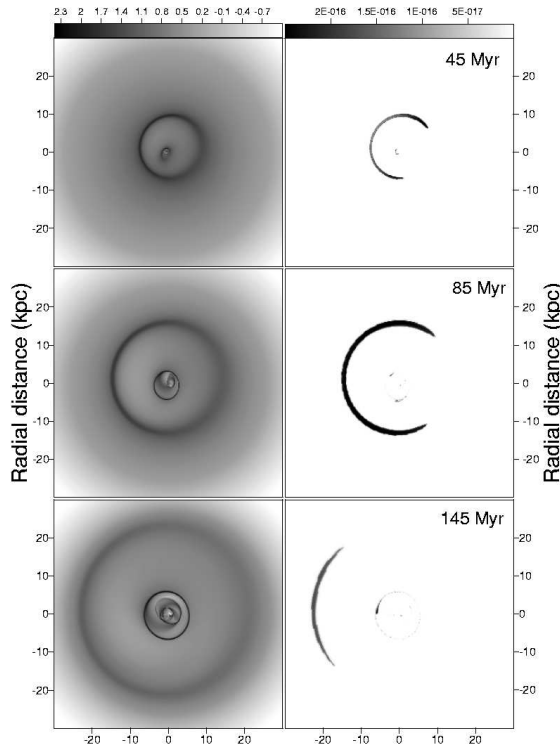


FIG. 17.— Model gas surface density (left) and  $H\alpha$  surface brightness (right) distributions at three consecutive times after the collision: 45 Myr, 85 Myr, and 145 Myr. The scale bars are in  $M_{\odot} \text{ pc}^{-2}$  (left) and  $\text{erg s}^{-1} \text{ cm}^{-2} \text{ arcsec}^{-2}$  (right)

characterized by  $Q < Q_{\text{cr}} = 1.6$ , while the rest of the outer ring has  $Q > Q_{\text{cr}} = 1.6$ . Significant azimuthal variations of the  $Q$ -parameter in the outer ring are easiest to reproduce by a slightly off-center collision (2.7 kpc), while a bull-eye central collision would require for more sophisticated physical conditions in the outer ring (e.g. systematic variations in gas temperatures along the ring perimeter). Thus we confirm that an off-center collision and star formation threshold are most probably responsible for the lack of  $H\alpha$  emission from the North-Eastern part of the Arp 10 outer ring, a conclusion previously made by Charmandaris et al. (1993). Our modeling predicts that the inner ring should be significantly less prominent in  $H\alpha$  than the outer ring. This seems to contradict the observations. We attribute this disagreement to the adopted gas isothermality in our numerical model – high gas densities in the inner ring might have invoked substantial cooling, which had lowered the gas temperature and associated star formation threshold.

It is interesting to consider the model-predicted temporal variations in the  $H\alpha$  surface brightness shown in Figure 17 (right frames). In the early phase of evolution, Arp 10 was less prominent in  $H\alpha$ , mainly due to a higher gas density and associated extinction in the expanding rings. At the present epoch, Arp 10 is likely to have reached a peak in the  $H\alpha$  surface brightness. In the next 20 Myr, Arp 10 is expected to fade in  $H\alpha$ , mainly due to a drop in the gas surface density of the outer ring. The radius of the stellar disk in Arp 10 at the  $\mu_B = 25 \text{ mag arcsec}^{-2}$  isophote is  $D_{25}/2 = 28 \text{ kpc}$ , according to RC3 (de Vaucouleurs et al. 1991). The middle-right panel in Figure 17 indicates that the present  $H\alpha$  ring in Arp 10 is located at about half the

radius of the stellar disk. This tendency was also found by Romano et al. (2007) for a sample of 15 northern ring galaxies. Thus we argue that a preferable location of  $H\alpha$  rings at half the stellar disk radius is probably caused by high extinction in the early expansion phase (which obscures  $H\alpha$  emission and hinders detection of small rings) and by a drop in the gas surface density below the star formation threshold in the later expansion phase. We caution that in the real systems there may be other mechanisms such as an interaction between rings and spiral density waves, which affect local star formation and  $H\alpha$  fluxes. We also note that the observed outer ring in Arp 10 has a noticeably larger eccentricity than the model outer ring. This is not a geometry effect because of low inclination of Arp 10 ( $i = 23^\circ$ ). We attribute a low eccentricity of our model outer ring to several factors. These are the two-dimensional nature of our modeling, initially axisymmetric distribution of gas in the disk of pre-collision Arp 10, and use of a fixed dark matter halo that cannot move in response to the companion.

#### 8.4. Global star formation rate

The gas-to-stellar mass ratio in Arp 10 is about 9% within a 50 kpc radius, which is typical for spiral galaxies. The global star formation rate (SFR) in Arp 10 can be estimated either from far-infrared (FIR) or  $H\alpha$  fluxes. The  $H\alpha$  flux is affected by the internal extinction, which according to § 5.1 may vary considerably across the disk of Arp 10. Therefore, we use the FIR fluxes taken from the NED database to estimate the FIR luminosity of Arp 10. The FIR fluxes of 0.784 Jy (60  $\mu\text{m}$ ) and 1.767 Jy (100  $\mu\text{m}$ ) suggest the FIR luminosity  $3.84 \times 10^{10} L_{\odot}$ . This value corresponds to the SFR of  $21 M_{\odot} \text{ yr}^{-1}$ , if a conversion factor between the FIR luminosity and SFR from Thronson & Telesco (1986) is used in combination with a Kennicutt (1983) initial mass function. We note that according to Zasov (1995) the conversion factor can be almost twice lower than the value derived by Thronson & Telesco (1986). Hence, we set a lower limit on the SFR in Arp 10 to be  $10 M_{\odot} \text{ yr}^{-1}$ . This value is still a factor of two larger than that derived by Charmandaris et al. (1993) using the  $H\alpha$  photometry. Romano et al. (2007) also found that SFRs estimated from FIR fluxes are also larger than those estimated from  $H\alpha$  fluxes. We attribute this difference to the internal extinction, which lowers  $H\alpha$ -estimated SFRs. The SFR in Arp 10 is very similar to that inferred by Mayya et al. (2005) for the Cartwheel.

On the other hand, our numerical simulations predict the present SFR in Arp 10 to be about  $6 M_{\odot} \text{ yr}^{-1}$ . If our FIR-based value of  $10 - 21 M_{\odot} \text{ yr}^{-1}$  is correct, it means that the star formation efficiency in Arp 10 is twice to four times more efficient than that derived by Kennicutt (1998) and used by us in equation (15). This elevated efficiency of star formation appears to be a common feature of ring galaxies. For instance, the Cartwheel galaxy is also characterized by a star formation efficiency three times larger than that of isolated and interacting galaxies in the Kennicutt's sample (Vorobyov & Bizyaev 2003).

Our numerical simulations indicate that the SFR in Arp 10 was a nearly linear function of time during the last 85 Myr. Hence, the present epoch SFR of  $10 - 21 M_{\odot} \text{ yr}^{-1}$  suggests that  $(4 - 9) \times 10^8 M_{\odot}$  of young stars were born as a result of the passage of the density wave.

This is less than 1% of the total stellar disk mass.

At the same time, Arp 10 has converted 3 – 6% of the total gas mass into stars. These values have to be certainly taken as lower limits for the star formation efficiency because only approximately half of the total gas content is located in the inner 16 kpc.

#### 9. LIMITATIONS OF OUR APPROACH

The spectral and numerical modeling of Arp 10 performed by us has several limitations and simplified assumptions, the impact of which on our results we discuss below. An assumption of constant propagation velocity of the rings made in § 5 contradicts numerical simulations (see e.g. Vorobyov & Bizyaev 2003). In the early evolutionary stage, the rings propagate faster than in the late stage. This tendency can be seen in Figure 8, which shows the azimuthal profiles of the gas expansion velocity in the outer ring at  $t=85$  Myr (solid line) and  $t=105$  Myr (dashed line) after the collision. The assumption of constant propagation velocity introduces additional uncertainty to the spectral modeling.

A faint signal and low-quality of long-slit spectra in the inter-ring region and behind the outer ring introduces an uncertainty in the spectral index modeling. Because of the adopted thin-disk approximation, we cannot model the vertical motions in the disk of Arp 10 after the collision, although these motions are well seen in the velocity fields in the inner parts of the galaxy. Ideally, a three-dimensional hydrodynamic model of Arp 10 should be combined with a population synthesis model, and the resulting model colors and spectra should be compared with observational data. High-resolution maps of gas density and internal extinction of Arp 10 would be needed in this case.

Nevertheless, the observed kinematics, spectral index modeling, and hydrodynamic modeling of Arp 10 are in general agreement. This suggests that we envision correctly a general picture of the collision and subsequent star formation in Arp 10. We postpone a more detailed numerical and spectral modeling to a future paper.

#### 10. CONCLUSIONS

We apply kinematic, spectral, and numerical approaches to develop a self-consistent model of propagating star formation in a collisional ring galaxy Arp 10. Our kinematic data have the best spatial resolution obtained for Arp 10 to date.

We found that the pre-collision Arp 10 was a large (Sb?) disk galaxy with an extended low surface density exponential stellar disk (scale length 7.2 kpc), substantial exponential bulge, and massive dark matter halo. The spiral arms that are traceable in our B-band and  $H\alpha$  images beyond the outer ring suggest that Arp 10 has had a spiral structure before the collision. Our spectral index modeling suggests the solar (using all selected indices or Mg, Ca, and Ti-related indices) or slightly sub-solar (using iron-dominated spectral indices) metallicity of the old stellar population in the center of Arp 10. The gradient of relative metallicity of the old population is  $-0.08$  dex  $kpc^{-1}$ .

The available measurements of the total hydrogen mass

and the shape of the rotation curve suggest high values of the Toomre  $Q$ -parameter ( $> 2.6$ ) in the pre-collision gas disk of Arp 10, which implies that star formation was moderated or even totally suppressed before the collision. The  $Q$ -parameter may decrease below a tentative stability limit of 1.6 if either a substantial undetected amount of molecular gas is present or the gas disk is highly concentrated to the center. Both possibilities appear to be unlikely. From the spectra of Arp 10 we estimate the oxygen abundance to be  $12+\log(O/H)=8.6$  with little variation along the radius.

Some 85 Myr ago an early-type spiral galaxy (Sab?) passed slightly off-center and near-axially through the disk of Arp 10. The velocity of the intruder galaxy was about  $800$   $km\ s^{-1}$  at the time of closest encounter and its mass was about  $1/4$  the mass of the target galaxy. The intruder is now seen as a small "knot" 5 arcsec to the South-West from the nucleus of Arp 10. The gravitational perturbation from the intruder generated two outwardly expanding density waves, which are presently seen in the B-band and  $H\alpha$  images as bright asymmetric rings. The expansion velocity of gas in the outer ring is a strong function of azimuth, with a maximum value of about  $110 \pm 10$   $km\ s^{-1}$  in the brightest part of the ring and a minimum value of about  $25 \pm 5$   $km\ s^{-1}$ . The inner ring has a more symmetric shape than the outer ring and expands with a velocity less than  $50$   $km\ s^{-1}$ . The propagating density waves in Arp 10 do not generate strong shock waves.

Star formation is triggered at the crest of an expanding gas density wave, if the gas surface density exceeds a star formation threshold. An apparent crescent-like distribution of  $H\alpha$  emission in the outer ring is most probably caused by a variation of the Toomre  $Q$ -parameter along the ring. The current star formation rate is estimated from the far-infrared flux to be  $10 - 21\ M_{\odot}\ yr^{-1}$ . The expanding waves of star formation have created less than 1% of the total stellar disk mass since the collision.

This project was partially supported by grants RFBR 04-02-16518, RFBR 05-02-16454, RFBR 06-02-16819-a, and Federal Agency of Education (project code RNP 2.1.1.3483). We are grateful to the anonymous referee for very useful comments and suggestions. This research is based on observations collected with the 6-m telescope of the Special Astrophysical Observatory (SAO) of the Russian Academy of Sciences (RAS), operated under the financial support of the Science Department of Russia (registration number 01-43.) This research has made use of the NASA/IPAC Extragalactic Database (NED) which is operated by the Jet Propulsion Laboratory, California Institute of Technology, under contract with the National Aeronautics and Space Administration. We acknowledge the usage of the HyperLeda database (<http://leda.univ-lyon1.fr>). E.I.V. acknowledges support from a CITA National Fellowship. Numerical simulations were done on the Shared Hierarchical Academic Research Computing Network (SHARCNET).

#### REFERENCES

- Afanasiev, V. & Moiseev, A. 2005, *Astron. Letters*, 31, 193, astro-ph/0502095
- Amram, P., Mendes de Oliveira, C., Boulesteix, J., & Balkowski, C. 1998, *A&A*, 330, 881

- Appleton, P. N. & Struck-Marcell, C. 1996, *Fundamentals of Cosmic Physics*, 16, 111
- Appleton, P. 1999, *Proc. IAU Symp. 186, "Galaxy Interactions at Low and High Redshift, Proceedings of IAU"*, Kyoto, Japan, 26-30 August, 1997. Ed. by J. E. Barnes, and D. B. Sanders, p.97
- Binney, J., & Tremaine, S. 1987, *Galactic Dynamics* (Princeton: Princeton Univ. Press)
- Bizyaev, D., Khoperskov, A. V., & Tiurina, N. 2003, *AAS*, 202, 40.13, astro-ph/0306193
- Bizyaev, D. & Kajsin, S. 2004, *ApJ*, 613, 886
- Block, D. L., Bournaud, F., Combes, F., Groess, R., et al. 2006, *Nature*, 443, 832
- Bohlin, R. C., Savage, B. D., & Drake, J. F. 1978, *ApJ*, 224, 132
- Borne, K.D., Appleton, P., Lucas, R., et al. 1997, *Rev. Mex. A.A.*, 6, 141
- Bottema, R. 1993, *A&A*, 275, 16
- Bransford, M. A., Appleton, P. N., Marston, A. P., & Charmandaris, V. 1998, *AJ*, 116, 2757
- Bruzual, G. & Charlot, S. 2003, *MNRAS*, 344, 1000
- Cardelli, J. A., Geoffrey, C. C., & Mathis, J. S. 1989, *ApJ*, 345, 245
- Chabrier, G. 2003, *PASP*, 115, 763
- Charlot, S. & Fall, M. 2000, *ApJ*, 539, 718
- Charmandaris, V., Appleton, P. N., & Marston, A. P. 1993, *ApJ*, 414, 154
- Charmandaris, V. & Appleton, P. N. 1996, *ApJ*, 460, 686
- de Vaucouleurs, G., de Vaucouleurs, A., Corwin, H. G., et al. "Third Reference Cat. of Bright Galaxies", Springer-Verlag: New York, (1991)
- Gallagher, J. S. III, Hunter, D. A., & Tutukov, A. V. 1984, *ApJ*, 284, 544
- Gonzalez Delgado, R.M., Leitherer, C., & Heckman, T.M. 1999, *ApJS*, 125, 489
- Gorgas, J., Cardiel, N., Pedraz, S., & Gonzalez, J. J. 1999, *A&ApSuppl*, 139, 29
- Hancock, M., Smith, B. J., Struck, C., et al. 2007, *AJ*, 133, 676
- Higdon, J.L. 1996, *ApJ*, 455, 524
- Higdon, J.L. 1996, *ApJ*, 467, 241
- Kennicutt, R.C. Jr. 1983, *ApJ*, 272, 54
- Kennicutt, R. C. Jr. & Kent, S. M. 1983, *AJ*, 88, 1094
- Kennicutt, R.C. Jr. 1998, *ApJ*, 498, 541
- Korchagin, V., Mayya, D., & Vorobyov, E.I. 2001, *ApJ*, 554, 281
- Kroupa, P. 2001, *MNRAS*, 322, 231
- Lynds, R. & Toomre, A. 1976, *ApJ*, 209, 382
- Markum, P.M., Appleton, P.N., & Higdon, L.J. 1992, *ApJ*, 399, 57
- Marston, A.P. & Appleton, P.N. 1995, *AJ*, 109, 1002
- Mayya, Y. D., Bizyaev, D., Romano, R., et. al. 2005, *ApJ*, 620L, 35
- McGaugh, S.S. & de Blok, W. J. G. 1997, *ApJ*, 481, 689
- Moiseev, A.V. 2000, *A&A*, 363, 843
- Moiseev, A.V. 2002, *Bull. SAO*, 54, 74, astro-ph/0211104
- Moiseev, A.V., Valdes, J.R., & Chavushyan, V.R. 2004, *A&A*, 421, 433
- Paturel, G., Petit, C., Prugniel, Ph., et al. 2003, *A&A*, 412, 45
- Pilyugin, L.S. & Thuan, T.X., 2005, *ApJ*, 631, 231
- Polyachenko, V. L., Polyachenko, E. V., & Strel'nikov, A. V. 1997, *Astronomy Letters*, 23, 483)
- Reshetnikov, V.P. 1999, *Astrophysics*, 41, 106
- Rolleston, W.R.J., Smartt, S.J., Dufton, P.L., & Ryans, R.S.I. 2000, *A&A*, 363, 537
- Romano, R., Mayya, Y. D., & Vorobyov, E. I., submitted to *AJ*
- Sandage, A. 1986, *A&A*, 161, 89
- Smirnov, M.A. & Komberg, B.V. 1978, *Sov. Astron. Letters*, 4, 133
- Smirnova, A.A., Moiseev, A.V., & Afanasiev, V.L. 2006, *Astronomy Letters*, 32, 520, astro-ph/0607163
- Thronson, H.A. Jr. & Telesco, C.M., 1986, *ApJ*, 311, 98
- Trager, S.C., Worthey, G., Faber, S.M., Burstein, D., et al. 1998, *ApJS*, 116, 1
- Stone, J.M. & Norman, M. L. 1992, *ApJS*, 80, 753
- van der Kruit, P. & Freeman, K. 1986, *ApJ*, 303, 556
- van Zee, L., Salzer, J.J., Haynes, M.P., O'Donoghue, A.A., et al. 1998, *AJ*, 116, 2805
- Vazquez G. & Leitherer C. 2005, *ApJ*, 621, 695
- Vorobyov, E. I. & Bizyaev, D. 2001, *A&A*, 377, 835
- Vorobyov, E. I., 2003, *A&A*, 407, 913
- Vorobyov, E. I. & Bizyaev, D. 2003, *A&A*, 400, 81
- Vorontsov-Veliaminov, B.A., 1976, *Sov. Astron. Letters*, 2, 204
- Wong, O. I., Meurer, G. R., Bekki, K., Hanish, D. J., et al. 2006, *MNRAS*, 370, 1607
- Worthey, G. 1994, *ApJS*, 95, 107
- Worthey, G. & Ottaviani, D. 1997, *ApJS*, 111, 377
- Zaritsky, D., Kennicutt, R.C. Jr., & Huchra, J.P. 1994, *ApJ*, 420, 87
- Zasov, A.V. 1995 *Astronomy Letters*, 21, 652
- Zasov, A.V. & Bizyaev, D.V. 1996, *Astronomy Letters*, 22, 71

TABLE 2  
EMISSION LINES IN ARP 10

$r$ , kpc	Fluxes in lines, in units of $10^{-16}$ erg s $^{-1}$ cm $^{-2}$						
	H $\beta$	H $\alpha$	[NII]6548	[NII]6584	[OII]3728	[OIII]5007	[OIII]4959
-1.36	8.52 $\pm$ 0.34	27.6 $\pm$ 0.32	2.93 $\pm$ 0.12	9.66 $\pm$ 0.15	2.74 $\pm$ 0.23	0.48 $\pm$ 0.12	—
1.36	8.06 $\pm$ 0.35	23.1 $\pm$ 0.28	4.43 $\pm$ 0.18	8.63 $\pm$ 0.14	2.36 $\pm$ 0.26	0.24 $\pm$ 0.06	—
11.59	4.60 $\pm$ 0.10	11.3 $\pm$ 0.14	1.10 $\pm$ 0.04	4.10 $\pm$ 0.07	4.53 $\pm$ 0.19	0.85 $\pm$ 0.04	0.22 $\pm$ 0.03
14.54	6.15 $\pm$ 0.09	21.4 $\pm$ 0.23	1.90 $\pm$ 0.03	7.98 $\pm$ 0.10	4.48 $\pm$ 0.15	2.51 $\pm$ 0.05	0.34 $\pm$ 0.02
16.36	2.67 $\pm$ 0.05	17.2 $\pm$ 0.19	1.37 $\pm$ 0.04	6.70 $\pm$ 0.09	1.19 $\pm$ 0.09	1.23 $\pm$ 0.04	0.23 $\pm$ 0.02

NOTE. — Emission line fluxes at different radii  $r$  in Arp 10.

TABLE 3  
EXTINCTION AND ABUNDANCES IN ARP 10

$r$ kpc	$P$	$A_V$ mag	12+log(O/H) dex	$f_{cor}(\text{H}\alpha)$ $10^{-15}$ erg s $^{-1}$ cm $^{-2}$	$f_{cor}(\text{H}\beta)$ erg s $^{-1}$ cm $^{-2}$
-1.36	0.132 $\pm$ 0.018	0.64 $\pm$ 0.03	8.57 $\pm$ 0.22	4.63 $\pm$ 0.34	1.61 $\pm$ 0.34
1.36	0.091 $\pm$ 0.017	0.00 $\pm$ 0.00	8.53 $\pm$ 0.28	2.31 $\pm$ 0.28	0.81 $\pm$ 0.35
11.59	0.190 $\pm$ 0.011	0.00 $\pm$ 0.00	8.53 $\pm$ 0.10	1.13 $\pm$ 0.14	0.46 $\pm$ 0.10
14.54	0.336 $\pm$ 0.010	1.01 $\pm$ 0.02	8.65 $\pm$ 0.06	4.88 $\pm$ 0.25	1.70 $\pm$ 0.09
16.36	0.320 $\pm$ 0.018	4.25 $\pm$ 0.09	8.62 $\pm$ 0.10	54.6 $\pm$ 1.16	19.0 $\pm$ 0.39

NOTE. — Extinction  $A_V$  in HII regions, excitation parameter  $P$  (see text), oxygen abundance 12+log(O/H), and H $\alpha$  and H $\beta$  fluxes corrected for the extinction ( $f_{cor}(\text{H}\alpha)$ ,  $f_{cor}(\text{H}\beta)$ ) in units of  $10^{-15}$  erg s $^{-1}$  cm $^{-2}$  at different radii  $r$  in Arp 10.